GERMANIUM ALLOYS FOR OPTOELECTRONIC DEVICES

A THESIS
SUBMITTED TO THE DEPARTMENT OF PHYSICS
AND THE INSTITUTE OF ENGINEERING AND SCIENCES
OF BILKENT UNIVERSITY
IN PARTIAL FULLFILMENT OF THE REQUIREMENTS
FOR THE DEGREE OF
MASTER OF SCIENCE

by
Ayşe Erbil
September 2008

I certify that I have read this thesis and that in my opinion it is fully adequate, in scope and in quality, as a thesis for the degree of Master of Science.

Prof. Dr. Atilla Aydınlı (Supervisor)

I certify that I have read this thesis and that in my opinion it is fully adequate, in scope and in quality, as a thesis for the degree of Master of Science.

Prof. Dr. Ahmet Oral

I certify that I have read this thesis and that in my opinion it is fully adequate, in scope and in quality, as a thesis for the degree of Master of Science.

Assoc. Prof. Dr. Oğuz Gülseren

Approved for the Institute of Engineering and Sciences:

Prof. Dr. Mehmet B. Baray
Director of Institute of Engineering and Sciences

ABSTRACT

GERMANIUM ALLOYS FOR OPTOELECTRONIC DEVICES

Ayşe Erbil
M.S. in Physics

Supervisor: Prof. Dr. Atilla Aydınlı
September 2008

Silicon has been the backbone of the mainstream electronics of the last fifty years. It is however, used in conjunction with other matierals, mainly with its oxides and nitrides. Germanium, on the other hand, is also a group IV element and has been used in the early stages of transistor and detector development. In addition to Si/Ge heterojunctions, bandgap engineering through SiGe alloys has also been used in photodetectors. Recent progress in light emitting devices utilizing Si nanocrystals suggest the use of $Ge_{1-x}N_x$ layers as barriers due to its suitable band offsets [1]. Experiments have shown that $Ge_{1-x}N_x$ is also a promising material for applications in photodiodes, amplifiers, optic fibers, protective coatings, etc [1]. Both Si and Ge are, however indirect bandgap semiconductors, lacking efficient light emission. On the other hand, strong light emission observed in Si nanocrystals has made the study of semiconductor nanocrystals an expanding field of interest due to potential applications in novel optoelectronic devices [2]. These nanocrystals exhibit strong luminescence and nonlinear optical properties that usually do not appear in the bulk materials [2]. SiGe nanocrystals attract attention due to the possibility of a tunable band gap with composition.

In this study, formation of $Ge_{1-x}N_x$ thin films and SiGe nanocrystals by plasma enhanced chemical vapor deposition (PECVD) reactor has been studied. We present the growth conditions and experimental characterization of the resulting thin films and nanocrystals. We used ellipsometry, Raman Spectrometry, Fourier Infrared Spectrometry (FTIR) and X-ray photoelectron Spectroscopy (XPS). For SiGe nanocrystals, 4 peaks in the Raman Spectra were observed around 295 cm^{-1}, 400 cm^{-1}, 485 cm^{-1} and 521 cm^{-1}. These peaks are assigned to the Ge-Ge, Si-Ge, local Si-Si and crystalline Si-Si vibrational modes, respectively [3]. For the $Ge_{1-x}N_x$ thin films FTIR spectrum showed the existence of the Ge-N bonds and its band offsets determined by XPS confirm its suitability for optoelectronic devices.

Keywords: Nanocrystals, PECVD, Raman Spectrometry, FTIR, XPS.

ÖZET

OPTOELEKTRONİK AYGITLAR İÇİN GERMANYUM BİLEŞİKLERİ

Ayşe Erbil
Fizik Bölümü Yüksek Lisans
Tez Yöneticisi: Prof. Dr. Atilla Aydınlı
Eylül 2008

Silisyum elektronik alanda geçen 50 yıla rağmen önemli bir yere sahiptir. Çoğunlukla silisyum oksit ve silisyum nitrat başta olmak üzere diğer maddelerle birlikte kullanılmaktadır. Diğer yandan, grup IV elementlerinden germanyum ise transistör ve detektör teknolojisinin başlangıç aşamalarında kullanılmaktadır. Si/Ge heterojunctionların yanı sıra, SiGe bileşikler fotodetektörlerde de kullanılmaktadır. Silisyum nanokristallerinin kullanıldığı ışık saçan aygıtlar üzerinde yapılan çalışmalar, bu diyotlarda uygun bant aralığına sahip olmasından dolayı $Ge_{1-x}N_x$ bileşiğinin bariyer olarak kullanılmasını öngörmüştür [1]. Ayrıca $Ge_{1-x}N_x$ bileşiğinin fotodiotlarda, elektronik yükselticilerde, optik fiberlerde kullanılan uygun bir madde olduğu bir çok deneyle gösterilmiştir [1]. Fakat bulk Si ve Ge maddelerinin dolaylı bant aralığına sahip olması, bu maddelerin ışık saçma verimliliğini düşürmektedir. Diğer bir yandan, kuvvetli ışık saçma özelliği gösteren Si nanokristaller optoelektronik aygıtların uygulamalarında kullanıldığı için yarı iletken teknolojisinde geniş ilgi alanına sahiptir [2]. Bu nanokristaller, bulk hallerinde görülmeyen kuvvetli ışıma ve linear olmayan optiksel özelliklere sahiptirler [2]. Ayrıca SiGe nanokristaller, bileşik kompozisyonu ile değişen enerji bant aralığına sahip oldukları için büyük ilgi görmüşlerdir.

Bu çalışmada, PECVD yöntemi ile oluşturulan SiGe nanokristaller ve $Ge_{1-x}N_x$ ince filmler incelenmiştir. Büyütme koşulları ve deneysel karakterizasyon yöntemleri incelenmiştir. Raman Spektrometre, elipsometre, Kızılötesi Spektrometre, X-ışınları fotoelektron Spektrometre yöntemleri ile maddelerin karakterizasyonu yapılmıştır. SiGe nanokristaller için 295, 400, 485, 521 cm^{-1} 'de 4 tane ayrı mod gözlenmiştir. Bu modlar sırası ile Ge-Ge, Si-Ge, l-Si-Si ve Si-Si modlarıdır [3]. Kızılötesi spektrometre ile Ge-N bağı, $Ge_{1-x}N_x$ ince filmlerde gözlenmiş ve XPS ile ölçülen band ofsetler $Ge_{1-x}N_x$ ince filmlerin optoelektronik aygıtlar için uygun olduğunu göstermiştir.

Anahtar Kelimeler: Nanokristaller, PECVD, Raman Spektrometre, Kızıl ötesi Spectrometre , X-ışınları fotoelektron Spektrometre.

Acknowledgements

I would like to thank my supervisor Prof. Dr. Atilla Aydınlı for his guidance, and support throughout the development of this thesis. I would also like to express my gratitude to Aydınlı group members Aşkın Kocabaş, İmran Akça, and doctoral students from Bilkent University Physics Department Münir Dede and Selcen Aytekin for their continuous support.

My special thanks is to Prof. Dr. Raşit Turan and his doctoral student İlker Yıldız, for the XPS measurements and Res. Ass. Prof. Dr. Aykutlu Dana for his encouragement during the course of this work. I would also acknowledge to Murat Güre and Ergün Karaman for their assistance and the facilities that we share at Advanced Research Labratory.

This work was funded by SEMINANO, a EU-FP6 project under the contract number 505285 and TUBITAK projects under the contract numbers 104M421 and 105T115.

I dedicate this thesis to my husband Caner Şan.

Table of Contents

1 INTRODUCTION ……..……..…..…….....*1*

2 SAMPLE PREPARATION……..……..…….....4

2.1 Thin Film Deposition with PECVD ……..……..…….....*4*

2.2 Preparation of $Ge_{1-x}N_x$ Thin Films …….....….....*6*

2.3 Preparation of $Si_{1-x}Ge_x$ Nanocrystals …….....*6*

3 CHARACTERIZATION OF $Ge_{1-x}N_x$ THIN FILMS *8*

3.1 Introduction *8*

3.2 Ellipsometric Characterization.....*8*

3.3 FTIR Spectroscopy Characterization .....…….....*10*

3.3.1 Introduction .....…….....*10*

3.3.2 Fundamentals of Infrared Absorption .....…….....*11*

3.3.3 Experimental Setup ... …….....…….....*12*

3.3.4 FTIR Spectroscopy of $Ge_{1-x}N_x$ Tin Films ….....…….....….....…...*13*

3.4 X-Ray Photoelectron Spectroscopy Characterization *17*

3.4.1 Introduction.…….....….....*17*

3.4.2 Basic XPS and Experimental Setup…….....*18*

3.4.3 XPS Analyses of the $Ge_{1-x}N_x$ Thin Films..….....…….....*19*

3.5 Band Offset Calculations.…….....*21*

4 CHARACTERIZATION OF $Si_{1-x}Ge_x$ NANOCRYSTALS…….....*27*

4.1 Ellipsometric Characterization ….....*27*

4.2 Raman Spectroscopy Characterization ….....….…*30*

4.2.1 Introduction *30*

4.2.2 Principles of Raman Scattering.…….....*30*

Phonon Confinement Effect.…….....….....*32*
Effects of strain and concentration.…….....…….....…….....*34*

4.2.3 Experimental Setup …….....*35*

4.2.4 Raman Spectrum Analyses of $Si_{1-x}Ge_x$ Nanocrystals …….....…….*37*

5 CONCLUSION AND FUTURE WORK ……..……..…....*49*

List of Figures

Figure 2.1.1 PECVD Reactor …….…....5

Figure 2.3.1 Two different multilayer structures of SiGe films grown by PECVD ..…….……..….....7

Figure 2.3.2 Single layer structure of SiGe films grown by PECVD.....7

Figure 3.2.1 Schematic setup of an ellipsometry experiment ……..…….....9

Figure 3.3.1 Schematic view of FTIR spectrum ……..……...13

Figure 3.3.2 Infrared absorbance spectrum of $Ge_{1-x}N_x$ thin films having 20 sccm (a) and 40 sccm (b) flow rates of GeH_4 with NH_3 flow rates of 50 sccm …….....…14

Figure 3.3.3 Raman spectrum of $Ge_{1-x}N_x$ thin films having 20 sccm(a) and 40 sccm (b) flow rates of GeH_4 with NH_3 flow rates of 50 sccm …….....15

Figure 3.3.4 Typical Raman spectrum of $Ge_{1-x}N_x$ thin films.....16

Figure 3.4.1 XPS spectrum of $Ge_{1-x}N_x$ thin films prepared with 20 sccm and 40 sccm flow rates of GeH_4 with NH_3 flow rates of 50 sccm. Shift of binding energy of Ge $2p_{3/2}$ (a) and N 1s (b).....20

Figure 3.5.1 Optical transmission spectrum of $Ge_{1-x}N_x$ thin films having 20 sccm and 40 sccm flow rates of GeH_4 with NH_3 flow rates of 50 sccm …….....….....22

Figure 3.5.2 Valence band energy spectrum of $Ge_{1-x}N_x$ thin films having 20 sccm and 40 sccm flow rates of GeH_4 with NH_3 flow rates of 50 sccm deposited for 20 min on SiO_2 (a) and Si (b) substrate ……..…….....23

Figure 3.5.3 Valence band energy spectrum of SiO_2 (a) and Si (b)……..24

Figure 4.1.1 The refractive index of the as grown and annealed (1200 ^oC for 30 min) Si_xGe_{1-x} films as a function of wavelength for samples having flow rates of 60 sccm (a) and 45 sccm (b) GeH_4.....28

Figure 4.1.2 Change in index of the Si_xGe_{1-x} nanocrystals as a function of wavelength for various flow rates of GeH_4 annealed at 1200 ^oC (a) and 1100 ^oC (b) for 30 min……..….29

Figure 4.2.1 Energy level diagrams of Rayleigh scattering, Stokes Raman scattering and anti-Stokes Raman scattering.....31

Figure 4.2.2 Detailed layout of the double monochromator used in the experiment……....36

Figure 4.2.3 Experimental setup used in the Raman experiments…….....36

Figure 4.2.4 Raman spectra of $Si_{1-x}Ge_x$ NC's sample 1(a) and sample (2) annealed at various temperatures for 7.5 min.....37

Figure 4.2.5 TEM images of the Sample 1 and Sample 2 $Si_{1-x}Ge_x$ NC.....39

Figure 4.2.6 Raman spectra of SiGe NC's samples having 30 sccm flow rates of GeH_4 annealed at 1200 ^oC (a) and 1100 ^oC (b) for various times…….…....41

Figure 4.2.7 Raman spectra of SiGe NC's samples having 45 sccm flow rates of GeH_4 annealed at 1200 ^oC (a) and 1100 ^oC (b) for various times…….....42

Figure 4.2.8 Raman spectra of SiGe NC's samples having 60 sccm flow rates of GeH_4 annealed at 1200 ^oC (a) and 1100 ^oC (b) for various times…….....43

Figure 4.2.9 Raman frequency of Ge-Ge mode of the SiGe nanocrytstals for annealed at 1100 ^oC and 1200 ^oC as a function of GeH_4 flow rates. 47

Figure 4.2.10 Raman spectra of SiGe NC's samples having 90 sccm and 120sccm flow rates of GeH_4 annealed at 1200 ^oC for 30 minutes……...……...48

List of Tables

Table 2.2.1 Growth parameters for $Ge_{1-x}N_x$ Thin Films.....6

Table 2.3.1 Growth parameters for SiGe Nanocrystals.....7

Table 3.2.1 GeH_4 flow rates dependence of refractive index and film thickness 10

Table 3.4.1 Measured Ge 3d and N1s binding energies.....20

Table 3.5.1 Calculated valence band and conduction band offsets for $Ge_{1-x}N_x$ thin films deposited on SiO_2 for different flow rates of GeH_4.....26

Table 3.5.2 Calculated valence band and conduction band offsets for $Ge_{1-x}N_x$ thin films deposited on Si for different flow rates of GeH_4 26

Table 4.2.1 Si-Ge modes in the Raman spectra of SiGe nanaocrystals in cm^{-1} 44

Table 4.2.2 Ge-Ge modes in the Raman spectra of SiGe nanaocrystals in cm^{-1} 44

Table 4.2.3 Si-Si local vibraitonal modes in the Raman spectra of SiGe nanaocrystals in cm^{-1} 44

Table 4.2.4 Ge concentration of $Si_{1-x}Ge_x$ nanocrystals.....45

CHAPTER 1: Introduction

Unlike its crystalline counterpart, Si nanocrystals (Si NCs) are known to exhibit strong visible light under photoexcitation. It has been shown that the spectral dependence of the emitted light is Si NC size dependent which provides additional flexibility in the design and realization of light emitting devices. This prompted the search for Si NC based electroluminescent devices to be used in Si based microelectronic platforms with the ultimate aim of achieving a Si NC based light emitters and ultimately an injection laser. Unfortunately, the intense search for efficient devices whether light emitting or laser have so far failed [4]. Many groups have demonstrated Si NC light emitting devices albeit with low efficiency [4]. Attempts to improve the efficiency have not been very successful. Typical structures investigated for Si NC based LEDs are composed of a thin layer of SiO_2 on a Si substrate with Si NCs embedded in it. Ohmic contact on the Si substrate side and a thin layer of metal or a transparent conducting oxide (TCO) on the oxide side completes the device. A band diagram of the device structure reveals that electrons from the TCO layer needs to tunnel into the Si nanocrystal states while holes need to be transported from the p-type Si substrate to the valance band states of the Si NC. Due to large band gap of SiO_2, a conduction band offset of 3.2 eV and even larger valance band offset of 4.2 eV develops on the Si side of the device which hinders the transport of holes to the SiO_2 valance band [5]. An intermediate layer with smaller band offset may facilitate hole injection into the Si NCs. Furthermore, it may also be used as the active layer with Si nanocrystals embedded in it.

Plasma enhanced chemical vapor deposition is the technique of choice for low cost light emitting devices. Thus, materials compatible with plasma enhanced growth may be good candidates for band-offset engineering of light emitting

devices. Among others a good candidate is grown a-$Ge_{1-x}N_x$:H using plasma enhanced chemical vapor deposition (PECVD) with GeH_4 and NH_3 as the gas precursors. In its crystalline form stochiometric germanium nitride (Ge_3N_4) is an insulator with a band gap of 4.7 eV [6]. It typically is found to contain both Ge_3N_2 and Ge_3N_4. Ge_3N_4 exists in both hexagonal and rhombic structure [1]. On the other hand, amorphous $Ge_{1-x}N_x$ can be grown using both CVD and PECVD deposition both of which are suitable for incorporation into light emitting structures. Many properties of amorphous a-$Ge_{1-x}N_x$: H films have been studied [1]. Band gap of a-$Ge_{1-x}N_x$ increases with nitrogen incorporation and reaches to 4.7 eV when N is greater than 50 atomic percent. The narrower band gap compared to SiO_2 offers the possibility of reduced band offset in the valance band edge when compared to SiO_2. Experimental determination of the valance and conduction band offsets of the $Ge_{1-x}N_x$ on Si and SiO_2 needs to be done in order to confirm this prediction.

In the literature, most of the group IV nitrides have been studied and data from these materials have been compared [1]. Nitrogen plays an important role for Group IV elements and germanium nitride, carbon nitride, silicon nitride and tin nitride have been studied. The band offset calculations of Si_3N_4 on Si were done with the same method described in Chapter 4. All results on crystalline silicon nitride studied by Xu et al. [7] and on germanium nitrides studied by Young et al. [8] have shown that nitride alloys have a great potential for applications in semiconductor technology.

On the other hand, the study of semiconductor nanocrystals is becoming an expanding field of interest due to potential applications in novel optoelectronic devices [2]. These nanocrystals exhibit luminescence and nonlinear optical properties that usually do not appear in bulk materials [2] so that they are being studied for applications in LEDs and flash memories as well as possible Si based lasers. Performance of these flash memories is influenced by NC shape and size, tunneling barrier thickness and control oxide thickness. The performance of data programming and retention in NC memory devices made of Ge NCs were recently proposed and tested [9-10]. However, Ge NCs based flash memories has higher

confinement barrier for retention and smaller barrier for program mode. Recent work [10] has suggested that SiGe NCs embedded in a suitable dielectric matrix may provide a more favorable band structure for these devices.

Due to the fact that bulk Si and Ge are indirect gap materials, both are poor light emitters restricting their use in the optoelectronic devices. However, the reduction of sizes down to the nanometer scale makes nanoscale Si efficient light emitters. While, emission wavelength of light from Si NC can be tuned with size from about 650 nm up to 1000 nm, it should also be possible to do so when Si is alloyed with the narrower band gap of Ge. Band structure of $Si_{1-x}Ge_x$ NC should depend both on composition and size and PL should be continously tunable from the shortest wavelength available from small nc-Si to those obtained from Ge NC. However, due to the significant differences between formation temperatures of Si and Ge nanocrystals, formation of $Si_{1-x}Ge_x$ nanocrystals are expected to be difficult.

In the literature, $Si_{1-x}Ge_x$ nanocrystals have been grown by magneton sputtering epitaxy, solid-phase crystallization, ion implantation, laser induced crystallization, molecular beam epitaxy [11]. Films grown by these techniques have been studied and it is shown that, main difference between them is the whether samples are stress free or not. $Si_{1-x}Ge_x$ formation by PECVD have not been studied widely.

In this study, formation of $Ge_{1-x}N_x$ thin films and of $Si_{1-x}Ge_x$ nanocrystals have been studied using plasma enhanced chemical vapor deposition (PECVD) techniques. Their properties are studied by ellipsometry, Raman spectroscopy, X-Ray photoelectron Spectroscopy (XPS), and Fourier Transform Infrared (FTIR) Spectroscopy.

CHAPTER 2: Sample Preperation

2.1 Thin Film Deposition with PECVD

The techniques to deposit thin films can be broadly classified into two groups: Chemical Vapor Deposition (CVD) and Physical Vapor Deposition (PVD) processes are basic deposition technologies. CVD is based on chemical reactions whereas PVD is evaporation of the materials in the form of atoms or molecules. The main categories of the PVD are vacuum evaporation, sputter deposition and ion plating. Each process has its own advantages, disadvantages and applications. For the growth of alloys, magneton sputter epitaxy, solid-phase crystallization, PECVD, metallorganicchemical vapor deposition, and ion implantation are most widely used techniques. In chemical vapor deposition, precursors are decomposed on the hot surface of the substrate, depositing the atom of interest on the surface. Due to the high temperatures used, the films that are grown are usually of high quality but this technique has high energy budget and is not desirable for production purposes. Instead, we have used a variant of chemical vapor deposition which uses lower temperatures but the decomposition process is assisted by an RF source. This technique is called PECVD.

In PECVD method, various gases are used and thin solid films are grown as a result of chemical reactions of these gases. Electrical excitation is used in PECVD to generate a glow discharge (plasma) and energy is transferred into molecules of the reactive radicals, ions, neutral atoms and molecules are created as a result of this excitation. They interact with the substrate and, depending on the nature of these interactions, either etch the substrate or deposit molecules on the substrate. Since the formation of the reactive and energetic species in the gas phase occurs by collision, the substrate can be maintained at relatively low temperatures. In other words, thin solid films can be grown at relatively low temperatures range between 150 ^{o}C and 350 ^{o}C.

This is the major advantage of PECVD. Other favorable properties of PECVD are good adhesion, low pinhole density, good step coverage and uniformity.

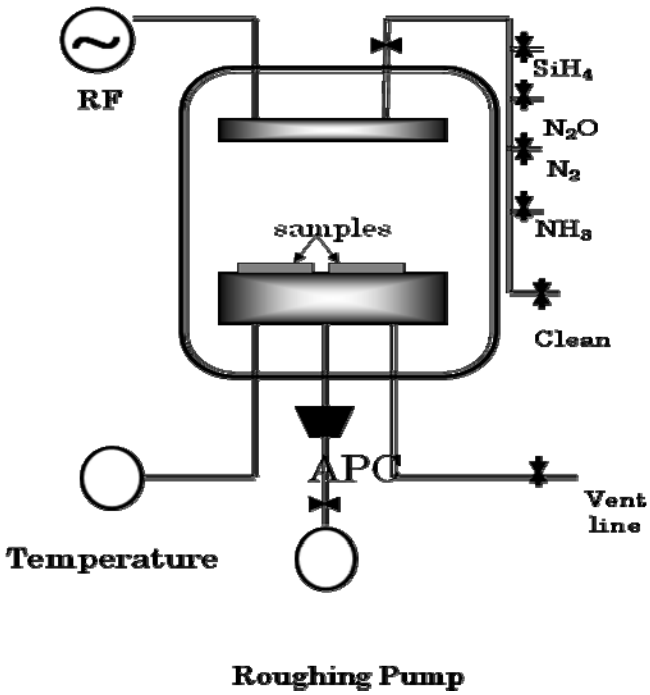

Figure 2.1.1. PECVD Reactor [12]

In our studies a PlasmaLab 8510C reactor is used to grow both $Ge_{1-x}N_x$ as well as SiO_x layers with excess Si and Ge. (Figure 2.1.1). There are two parallel plate electrodes and the radio frequency (RF) generated plasma are between these two plates. The RF power is applied to the upper electrodes and system is heated up to 350 ^oC from the ground electrodes where the samples are placed. The working pressure and RF power can be changed between 100-1000 mTorr and 12-300 Watts, respectively. Precursors gases used in PECVD are silane (2% SiH_4/N_2), amonia (NH_3), nitrous oxide (N_2O) and germane (2% GeH_4/He).

2.2. Preparation of $Ge_{1-x}N_x$ Thin Films

Various $Ge_{1-x}N_x$ films were deposited on silicon (100) wafers, quartz and with 4 nm thermal oxide using PECVD reactor (Figure 2.1.1) using the gas mixtures of NH_3 and GeH_4. For all samples, the flow rate of NH_3 was fixed at 50 sccm and various flow rates of GeH_4 were performed (Table 2.2.1). The working pressure was maintained at 1000 mTorr and RF power was 12 W. The temperature of the substrate was fixed at 250 ^oC. Annealing was performed at various temperatures up to 800 ^oC for 10 min under N_2 ambient atmosphere.

NH_3	50 sccm
GeH_4	20-40 sccm
Temperature	250 ^0C
Pressure	1000 mTorr
RF Power	12 W

Table 2.2.1. Growth parameters for Ge1-xNx Thin Films

2.3. Preparation of $Si_{1-x}Ge_x$ Nanocrystals

First, SiO_2/a-Ge/a-Si/SiO_2 multilayers were deposited on silicon (100) wafers using a PECVD reactor (Figure 2.3.1) using the gas mixture of SiH_4, N_2O and GeH_4. Care was taken to deposit a-Si and a-Ge as thin as possible. The flow rates of SiH_4, N_2O and GeH_4 were 200 sccm, 180 sccm, and 200 sccm, respectively. The working pressure was maintained at 1000 mTorr and RF power was 12 W. The temperature of the substrates was fixed at 350 ^oC.

Sample 1		Sample 2	
SiO_2	150 nm	SiO_2	150 nm
SiO_2	15 nm	SiO_2	15 nm
a-Ge	10 nm	a-Si	8 nm
a-Si	8 nm	a-Ge	10 nm
SiO_2	15 nm	a-Si	8 nm
SiO_2	150 nm	SiO_2	15 nm
Si substrate		SiO_2	150 nm
		Si substrate	

Figure 2.3.1: Two different multilayer structures of the SiGe films grown by PECVD.

Alternatively, multilayers of SiO2 with various amounts of excess Si and Ge were deposited on silicon (100) wafers using the same PECVD reactor as a single layer using gas mixture of SiH_4, N_2O and GeH_4. The flow rates of SiH_4, N_2O were fixed at 220 sccm, 8 sccm, respectively and various flow rates of GeH_4 (120, 90, 60, 45, 30, 15 sccm) were used (Table 2.3.1). Working pressure was maintained at 1000 mTorr and RF power was 12 W. The temperature of the substrates was fixed at 350 ^oC. Annealing process was performed at 1100 ^oC, and 1200 ^oC for 30, 45, and 60 minutes under N_2 ambient atmosphere.

SiH_4	220 sccm
N_2O	8 sccm
GeH_4	120-90-60-45-30-15 sccm
Temperature	350 ^0C
Pressure	1000 mTorr
RF Power	12 W

Table 2.3.1.Growth parameters for SiGe Nanocrystals

Sample Type 3
SiO_2:Si:Ge
SiO_2
Si substrate

Figure 2.3.2: Single layer structure of SiGe films grown by PECVD

CHAPTER 3: Characterization of $Ge_{1-x}N_x$ Thin Films

3.1. Introduction

The electrical and optical properties of semiconductors depend on their composition and structure [7]. Si based amorphous compounds have been extensively studied and they are considered as promising materials for photoelectronic devices [13]. On the other hand, Si nanocrystal based MIS-LED is being studied intensively. However, injection of electrons and holes into nanocrystal MIS-LEDs is difficult, making the choice of materials with appropriate bandgaps and band offsets important. Recent work showed that amorphous germanium-nitrogen compounds form the alloy $Ge_{1-x}N_x$, a wide band gap insulator. Thus, $Ge_{1-x}N_x$ alloys may be good candidates as gate dielectric materials for metal-insulator-semiconductor (MIS) structures providing much favorable tunable band offsets [13].

For the purpose of this work, formation of $Ge_{1-x}N_x$ films and optical and electronic characterization of these films are studied by ellipsometry, Fourier Transform Infrared (FTIR) spectroscopy and X-Ray Photoelectron spectroscopy (XPS). Also, band offsets calculations are performed for $Ge_{1-x}N_x$ films on Si and SiO_2.

3.2. Ellipsometric Characterization

Index and thickness measurements were performed on as deposited samples using ellipsometry at 632 nm. Ellipsometry measures the changes of polarization upon reflection or transmission. This means that a known polarization is reflected or transmitted and the output polarization is measured. The change in the polarization can be written as [14];

$$\rho = \tan(\psi)\, e^{i\Delta} \qquad 3.2.1$$

where ρ is the ration of the s and p polarizations, tan(ψ) amplitude ratio of reflection and Δ is the phase shift difference. The dielectric function of the material can be found as;

$$\epsilon = \sin^2\emptyset + \sin^2\emptyset\tan^2\emptyset\left[\frac{1-\rho}{1+\rho}\right]^2 \qquad 3.2.2$$

where $\emptyset$ is the angle of incidence. From the dielectric function, index of refraction can be determined by the formula given below:

$$\epsilon = n^2 \qquad 3.2.3$$

The basic working principle of ellipsometry is shown in Figure 3.2.1 schematically. Light polarized by the polarizer passes from the compensator or phase modulated and is reflected by the sample. Reflected light passes through the analyzer and is detected by the detector.

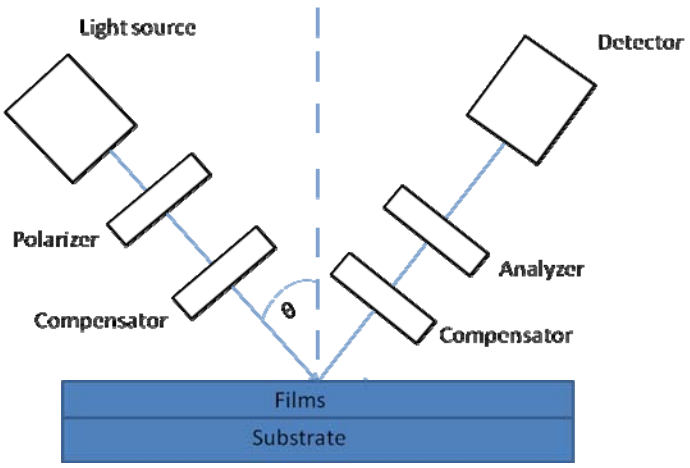

Figure 3.2.1: Schematic setup of an ellipsometry experiment.

Table 3.2.1 shows index and thickness values with changing flow rates of GeH_4. As flow rate increase, both thickness and refractive index increase.

GeH4 Flow Rates	Growth Time	Thickness	Index
(sccm)	(min)	(nm)	
20	10	49.1	2.00
20	20	92.7	2.10
30	10	65.3	2.02
30	20	123	2.13
40	10	84.1	2.10
40	20	129	2.30

Table 3.2.1: GeH_4 flow rates dependence of refractive index and film thickness

The data we obtained from our films is given in Table 3.2.1. We have grown samples with flow rates of 20, 30 and 40 sccm of GeH_4 while the flow rate of NH_3 was kept constant at 50 sccm. The growth times were either 10 min or 20 min. We note that there is a general trend of increasing index with increasing GeH_4 flow rate. It is also notable that samples grown for 10 min and those grown for 20 min form subgroups. In another words, if we just look at the samples grown for 10 min. we find a clear indication of increasing index of refraction with increasing GeH_4 flow rates just as is the case for the samples grown for 20 min. However, there is a small difference between samples grown with the same flow rates but different lengths of time. This suggests a small inhomogenity develops as the thickness of the samples increase. Experimentally obtained refractive index values confirm the formation of $Ge_{1-x}N_x$ and measured indices are in agreement with literature [13-15].

3.3. FTIR Spectroscopy Characterization

3.3.1. Introduction

Infrared spectroscopy is the most commanly used technique to analize materials. An infrared spectrum represents characteristics of samples with absorption peaks which correspond to the frequencies of vibrations of molecules. Because each material is a unique combination of atoms, no two compounds produce the exact same infrared spectrum. Therefore, infrared spectroscopy can provide in a positive qualitative analysis for different kinds of material. It can identify unknown

materials, determine the quality of the sample and the amount of molecules in a mixture. Furthermore, FTIR is a non-destructive method that requires no external calibration.

Fourier Transform Infrared (FTIR) spectroscopy is employed to confirm the existence of $Ge_{1-x}N_x$ film and to characterize the formation conditions of this film. In this seciton, first the theoretical background is given, and than experimental set up is described, finally the experimental results are discussed.

3.3.2. Fundamentals of Infrared Absorption

Absorption of infrared energy occurs due to light coupling between vibrations or rotations of atoms in molecules. Molecules can absorb infrared light when its dipole moment change due to vibrations or rotations. If the electric field of light, interacts with the fluctuations in dipole moment and has frequency of radiation that matches with normal vibrational or rotational modes of the molecule, than infrared radiation can be absorbed by the molecule. This is the basis of the infrared absorption [16].

Classical theory of vibration of molecules can be described according to harmonic binding potential [17]. The vibrational frequency can approximately be estimated by solving simple one dimensional spring systems. As a result of this approach, the energy of absorption peak for diatomic molecules with different masses may be estimated as;

$$E = \frac{1}{2\pi}\sqrt{\frac{K}{\mu}} \qquad 3.3.1$$

In quantum mechanical treatment the energy the same can written as;

$$E = (\omega + \frac{1}{2})\frac{h}{2\pi}\sqrt{\frac{K}{\mu}} \qquad 3.3.2$$

where K is the spring constant, ω is the frequency of absorption and μ is the effective mass of the system. As a simple rule of thumb, as the effective mass of the system increases, vibrational frequency shifts to lower wavenumbers.

3.3.3. Experimental Setup

FTIR spectroscopy is an optical characterization technique used in the infrared region of the electromagnetic spectrum. Principle of FTIR spectrophotometer operation is very similar to the Michelson interferometer (Figure 3.3.1). In this spectrophotometer, radiation from the light source is divided into two by a beam splitter. These two beams of the radiation is reflected from movable and fixed mirrors, respectively and then combined at beam splitter. This radiation reflected from or transmitted through the sample and is focused on a detector. Due to different positions of movable mirror, there is a path difference between the two waves and a time delay occurs. The intensity of light measured at the detector is [18];

$$I(\Delta s) = \int_0^\infty I(w)\ \cos(2\pi w \Delta s)\, dw \qquad 3.3.3$$

where I(w) is the radiation intensity reflected or transmitted through the sample and Δs is the path dfference between the beams. The measured signal is digitized and sent to the computer where the Fourier transformation is performed. The Fourier transform of equation 3.3.3 gives the spectra of transmitted intensity as a function of wavenumber as;

$$I(w) = 2\, Re \int_0^\infty I(\Delta s) \cos\,(2\pi w \Delta s)\, d\Delta s \qquad 3.3.4$$

Because there needs to be a relative scale for the absorption intensity, a background spectrum must also be measured. This is normally a measurement with

no sample in the beam. Comparasion between background signal and sample signal is made and results in a spectrum which has all of the instrumental characteristics removed is obtained.

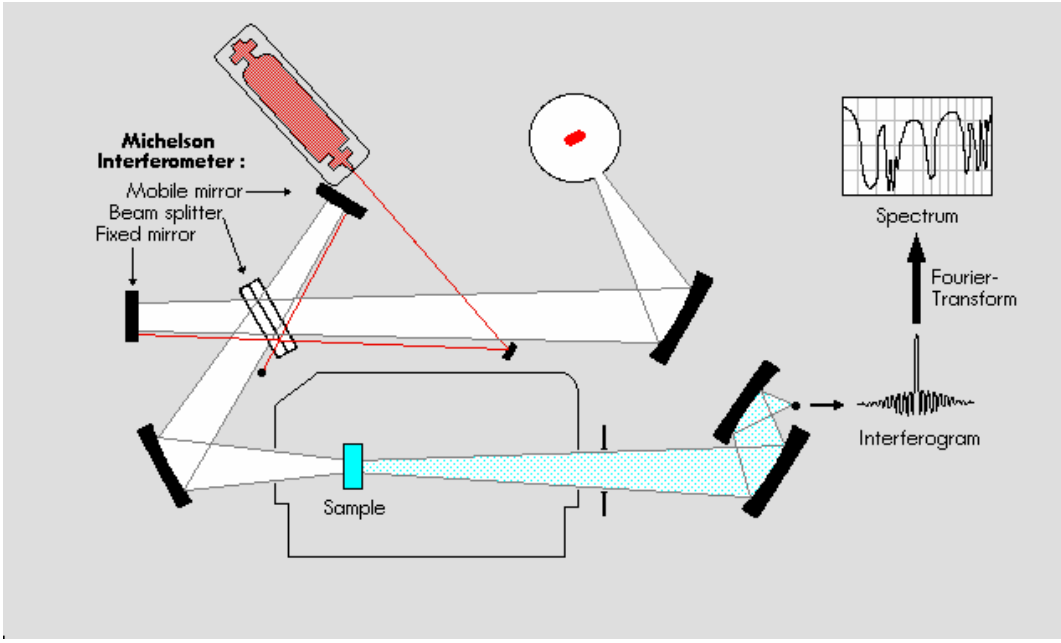

Figure 3.3.1: Schematic view of FTIR spectrum (adapted from BOMEM)

3.3.4. FTIR Spectroscopy of $Ge_{1-x}N_x$ Thin Films

$Ge_{1-x}N_x$ films were deposited on double side polished silicon (100) wafer using the gas mixtures of NH_3 and GeH_4. Samples, having flow rate of 50 sccm NH_3 and flow rates of 20 sccm and 40 sccm GeH_4 were subjected to Fourier Transform Infrared (FTIR) spectroscopy. For as-grown samples having flow rates of 20 sccm GeH_4 only one absorption band, centered at 736 cm^{-1} are measured. This peak is assigned to well known Ge-N vibrational mode [19]. When this sample is annealed at 800 ^oC for 15 min, absorption band centered at 730 cm^{-1} is observed in the spectrum. For further annealing at high temperatures, absorption band disappears due to degradation of Ge-N bonds and desorption of N from $Ge_{1-x}N_x$ films (Figure 3.3.2 a). For samples having flow rate of 40 sccm GeH_4, absorption band occurs at

730 cm^{-1} and 731 cm^{-1} for as grown sample and sample annealed at 800 ^{o}C, respectively (Figure 3.3.2 b).

To check the stability of the thin films, we heated the samples in a furnace at temperatures up to 900 ^{o}C for 10 min under nitrogen atmosphere. We found that the spectrum conserves its shape and the central frequency while its absorbance decreases by a small amount. This suggests that the samples are still intact. However when the temperature is raised to 900 ^{o}C the absorption signal is lost altogether indicating that the film has decomposed.

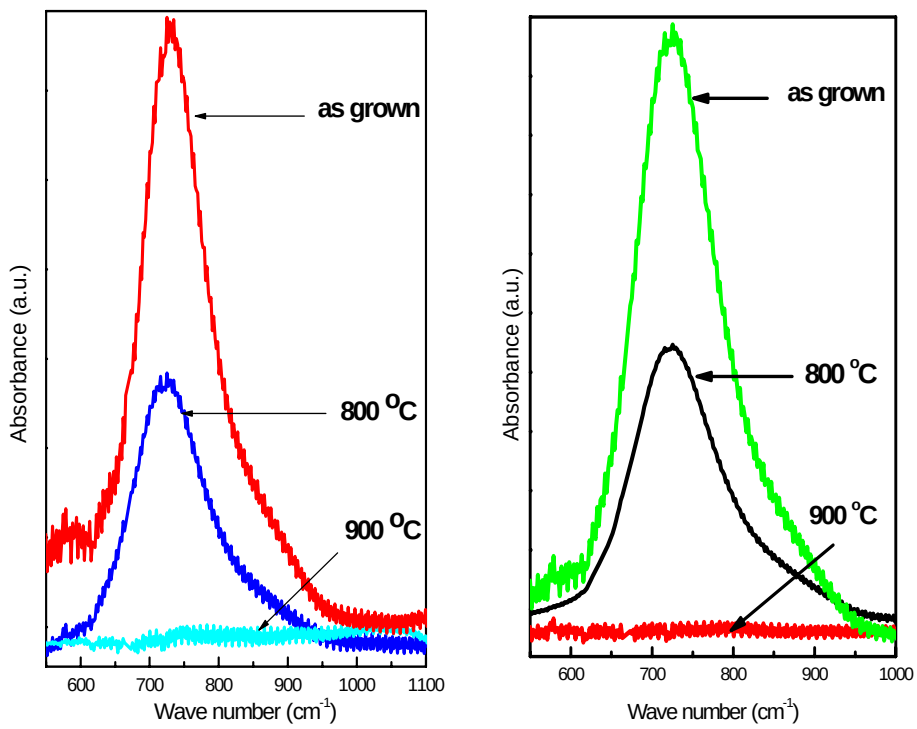

(a) (b)

Figure 3.3.2: Infrared absorbance spectrum of $Ge_{1-x}N_x$ thin films having 20 sccm (a) and 40 sccm (b) flow rates of GeH_4 with NH_3 flow rates of 50 sccm.

Electronegativity of nitrogen is higher than the germanium. Thus increasing N concentration leads to increase in vibrational frequency due to electron charge transfer from germanium to nitrogen [13]. On the other hand, increasing in N concentration reduces total mass of the system and gives rise to increase in

vibrational frequency according to vibrational frequency equation derived above since Ge is heavier atom than N. Ge-N bonds observed in Figure 3.3.2 shift with changing Ge concentrations and annealing temperatures. Even though N concentration is fixed, absorption peak shifts (~5 cm^{-1}) to lower wavenumbers with increasing Ge concentration. Increase in Ge concentration reduces the concentration of N, extends the Ge-N bond length, and decreases the force and vibrational frequency [1]. Samples grown with different GeH_4 flow rates do not show significant changes. The observed shift in our experiment is relatively small indicating that the concentration of N does not change significantly in the $Ge_{1-x}N_x$ thin films.

At 800 ^oC Ge-N bonds start to degrade. Total mass increases, vibration frequency shifts to lower wavenumbers. At temperatures higher than 800 ^oC, no absorption band is measured due to total desorption of N atoms as is seen also in the Raman spectrum of the samples (Figure 3.3.3).

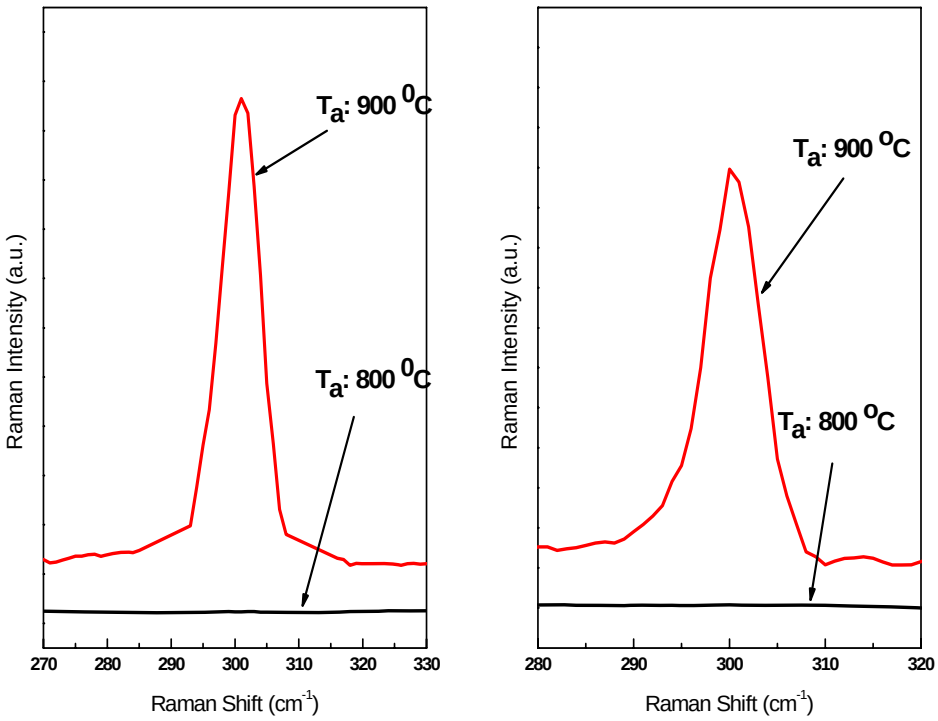

(a) (b)

Figure 3.3.3: Raman spectrum of $Ge_{1-x}N_x$ thin films having 20 sccm (a) and 40 sccm (b) flow rates of GeH_4 with NH_3 flow rates of 50 sccm.

Thus, the FTIR spectrum confirms the existence of $Ge_{1-x}N_x$ thin films. All as grown and annealed samples have an absorption line at around 730 cm^{-1} in the IR spectrum. This infrared transmission analysis of the films suggests that films contain amorphous germanium nitride.

Raman spectroscopy provides complementary information to infrared spectroscopy. We, therefore, studied the same $Ge_{1-x}N_x$ films with Raman spectroscopy and the results are shown in Fig. 3.3.3.As grown samples deposited with 20 and 40 sccm GeH_4, both show no peaks for $Ge_{1-x}N_x$ films. Figure 3.3.4 shows the typical Raman spectrum of the $Ge_{1-x}N_x$ thin films [20].

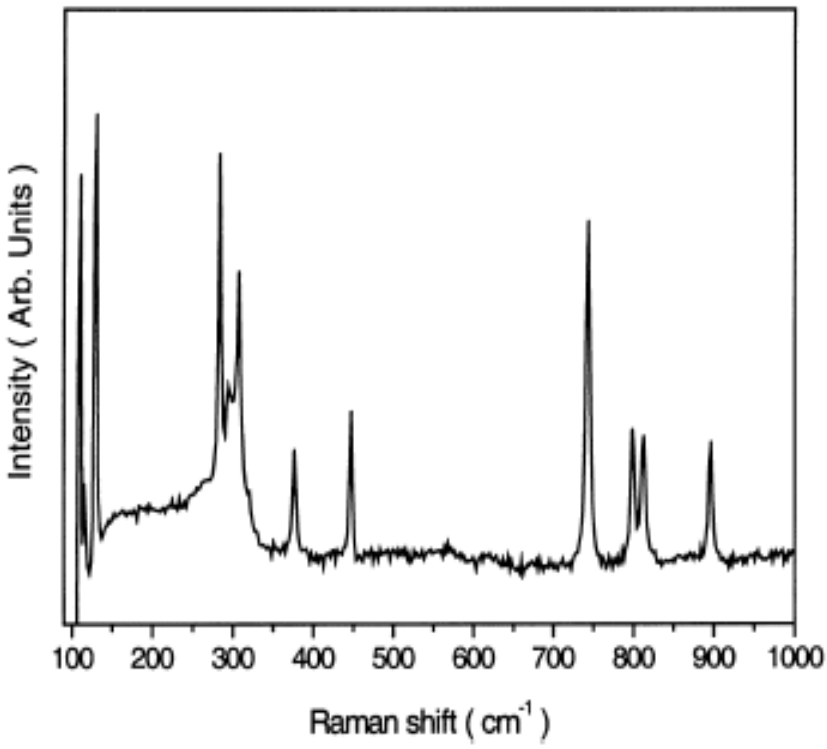

Fig. 3.3.4. Typical Raman spectrum of $Ge_{1-x}N_x$ thin films

All Ge-N modes are clearly identified. Unfortunately, we did not observe any one of these modes in the Raman spectra of as grown $Ge_{1-x}N_x$ films even when annealed up to 800 ^oC. This may be due to thin transparent nature of the films.

Since the films are very thin and higly transparent, the laser line is not absorbed leading to effectively small scattering volume.

However, when annealed at 900 ^{o}C but display a prominent peak that corresponds to Ge-Ge mode at higher annealing temperatures. This observation of the optical phonon of the Ge at approximately 300 cm^{-1}, clearly indicates the formation of crystalline germanium due to decomposition of $Ge_{1-x}N_x$ films.

3.4. X-ray Photoelectron Spectroscopy Characterization

3.4.1. Introduction

X-ray Photoelectron Spectroscopy (XPS) is a powerfull and very sensitive technique in determining elemental composition and chemical state of materials. It is surface sensitive technique which collectes the information from a thickness of a few nm (3-10 nm) from the surface of the material. One of the interesting applications of XPS is to determine the electronic band-offsets formed between very thin surface layer and the substrate. It is based on measurement of kinetic energy of electrons ejected from the surface upon irradiation by an x-ray beam. During XPS measurement, the material's surface is irradiated by an x-ray beam whose energy is transferred to the electrons which are then excited to free space with an energy which is proportional to characteristic binding energy. Each element has a characteristic binding energy value for its core electrons. The binding energy is also very sensitive to the chemical environment of the element, which is the chemical bonding with neighboring atoms. Thus, measuring the binding energy of ejected electrons (photoelectrons) provides information on identity of the chemical element as well as its bonding with other elements. In addition to chemical information obtained from the core electrons, XPS has been shown to be useful in determining electronic band-offsets formed on the surface of the material [21]. Band offset is determined from the measurement of binding energy of valence

electrons which are loosely bound to the atoms. The binding energy of valence electrons are usually are usually very small and thus difficult to measure with XPS. It requires careful measurement and evaluation of the data.

In this thesis, $Ge_{1-x}N_x$ films were characterized by X-ray photoelectron spectroscopy (XPS) to find out composition and electronic structure. Both core electrons and valence electrons were analyzed for this purpose. Below, following brief information about theory of XPS and experimental set up XPS study of $Ge_{1-x}N_x$ films are presented and results are discussed.

3.4.2. Basic XPS and Experimental Setup

When samples are irradiated by x-rays, x-ray photon is absorbed by an atom and inner (core) shell electrons are emitted. The kinetic energy, E_k, of these photoelectrons is determined by the energy of the x-ray radiation, hυ, and the electron binding energy, E_b, as given by [22]:

$$E_k = h\upsilon - E_b - Q \qquad 3.4.1$$

where Q is the spectrometer work function.

XPS systems contain a X-Ray source, an ultra-high vacuum chamber, and electron energy analyzer. Samples mounted in the system are irradiated by the x-rays obtained by electron irradiation of various metallic targets. Monochromatic X-rays from an aluminum target can provide K-alpha X-rays with photon energy of 1486.7 eV. Magnesium targets with photon energy of 1253 eV are also used. Samples are placed in an ultra-high vacuum chamber. Ultra-high vacuum is necessary for photoelectrons not to be absorbed by the air molecules before they reach the electron energy analyzer.

While working with XPS, one must consider the charging effect of the samples under study. Charging effect may cause the shifting of the all peaks observed an X-ray photoelectron spectrum [23]. For calibration, as commonly applied, C 1s energy

was measured and compared with known energy value of 284.5 eV. In our experiments, for all samples, measured values were corrected with respect to C 1s energy line.

3.4.3. XPS Analyses of the $Ge_{1-x}N_x$ films

In this study, $Ge_{1-x}N_x$ films were characterized by XPS. Depth profiling was done using argon ion beam at an energy of 1500 eV.

The XPS measurements showed that the surface of the films were oxidized. However, upon Ar ion sputtering for a few minutes, oxygen free films containing both Ge and N were observed. Samples annealed up to 800 ^{o}C did not show noticeable differences from as-grown samples indicating high stability of the films. Figure 3.4.1 shows binding energy of Ge $2p_{3/2}$ electrons and N 1s electrons. Ge $2p_{3/2}$ peaks are clearly seen at 1215.8 eV and 1216.6 eV for the films having 20 sccm and 40 sccm flow rates of GeH_4, respectively. Bulk Ge has $2p_{3/2}$ line at 1217 eV [24]. A chemical shift of 1.2 eV seen for the lowest Ge concentration decreases to 0.4 eV with increasing Ge concentration in the films. N 1s peaks are observed at 397.2 eV and 397.3 eV for the films having 20 sccm and 40 sccm flow rates of GeH_4, respectively. For atomic N 1s is given at 398.1 [13]. A shift of 0.9 eV and 0.8 eV are measured for these two samples. These shifts are usually attributed to the electronegativity differences between Ge and N atoms [25].

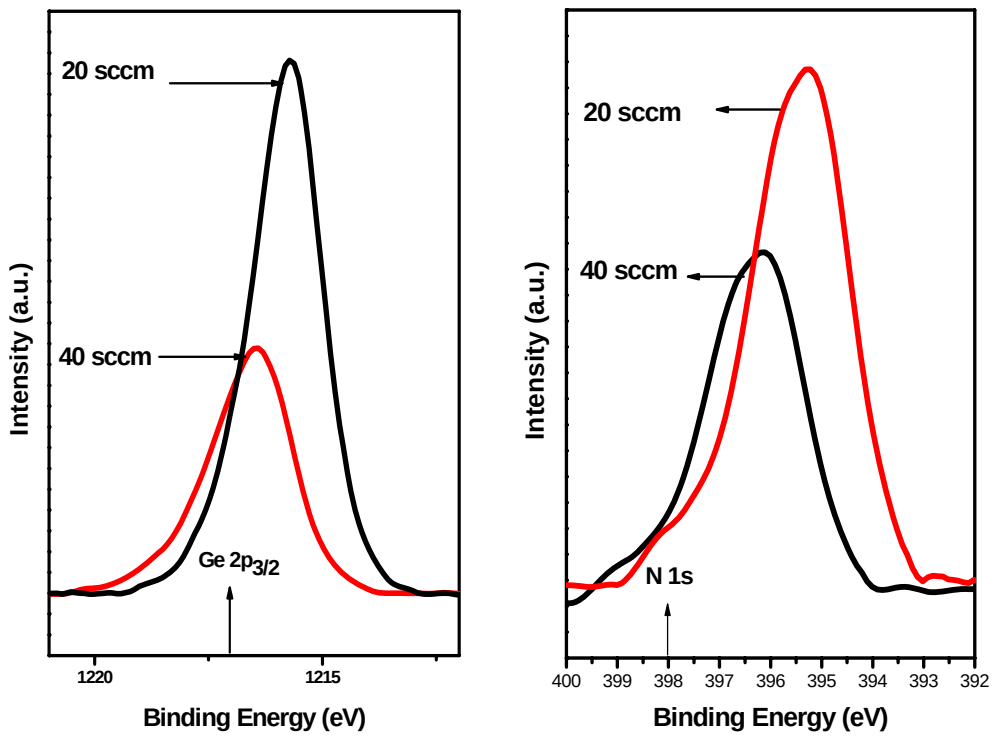

(a) (b)

Figure 3.4.1. XPS spectrum of $Ge_{1-x}N_x$ thin films prepared with 20 sccm and 40 sccm flow rates of GeH_4 with NH_3 flow rates of 50 sccm. Shift of binding energy of $Ge2p_{3/2}$ (a) and N 1s (b)

GeH_4 flow rates (sccm)	Ge 3d (eV)	N 1s (eV)	N 1s – Ge 3d (eV)
20	32,9	398,8	365,9
40	33,2	399,0	365,8

Table 3.4.1: Measured Ge 3d and N1s binding energies

For further analyses, Ge 3d line is measured. Same shifts as those observed in the case of Ge $2p_{3/2}$ line are observed. This can be understood by considering electron exchange between atoms [13]. The difference between the core level

electron energy of Ge (3d=29.4 eV) and N (1s=398.1 eV) must be 368.7 eV if there is no electron transfer between them. Table 3.4.1 shows binding energy of Ge 3d and N 1s. The difference between binding energies is smaller than 368.7 eV meaning that electron is transferred from germanium to nitrogen atoms. There is however, little difference between samples grown with different GeH_4 flow rates indicating that there is no bonding difference between the two samples.

3.5. Band Offset Calculations

The first step in the determination of the band offsets is the determination of the band gap of $Ge_{1-x}N_x$. The band gap of the $Ge_{1-x}N_x$ films was measured by an optical transmission experiment using an optical ellipsometer. Figure 3.5.1 shows the transmission spectrum of $Ge_{1-x}N_x$ films prepared with 20 sccm and 40 sccm flow rates of GeH_4. Band gaps of $Ge_{1-x}N_x$ films were calculated as 4.78 eV and 4.57 eV from these spectra. Band gap of $Ge_{1-x}N_x$ films are reported to be approximately 4.5 eV [25-26]. As N concentration increases the energy bang gap increases from 4.5 eV to 4.7 eV. Addition of excess N causes structural disorder [7] in the system, dipole moments change and band gap energy changes, since Ge-N bond energy is larger than the Ge-Ge bond energy [13].

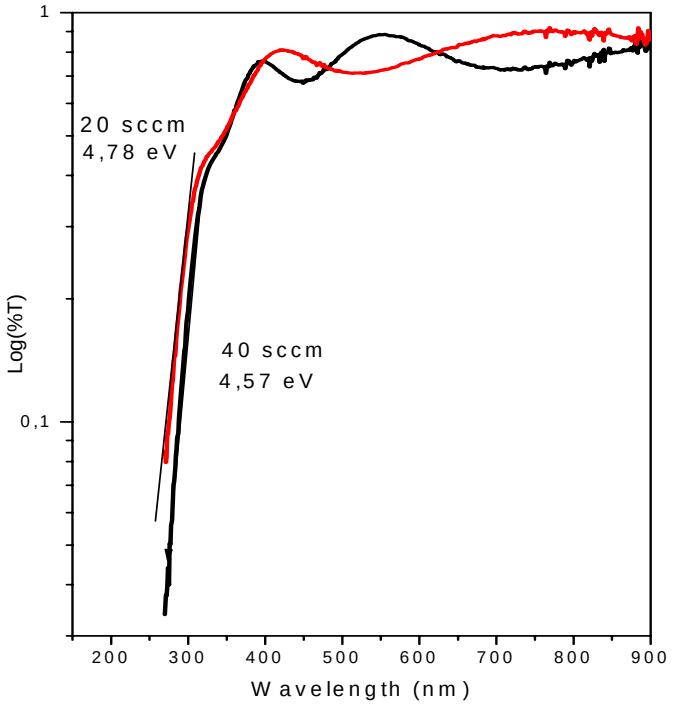

Figure 3.5.1: Optical transmission spectrum of $Ge_{1-x}N_x$ thin films having 20 sccm and 40 sccm flow rates of GeH_4 with NH_3 flow rates of 50 sccm.

After the determination of band gap energies, valence band measurements were performed for $Ge_{1-x}N_x$ films grown on thermal oxide and Si substrate with XPS.

XPS has previously been used to determine band alignment of the dielectric/semiconductor structures [24]. Valence band edge of a material can be obtained directly from XPS measurements [21]. This technique is based on the determination of the intercept of the line fitted to the lower energy part of the valence electron's peak [27]. We have employed this method to determine the valence band edge of the $Ge_{1-x}N_x$ films we fabricated. Intersection point on the energy axis gives the valence band edge of the respective material. Using this method and taking into account the charging effect, measured valence band graphs for samples deposited for 20 minutes on thermal oxide and Si substrates are shown

in Figure 3.5.2. For the samples grown on thermal oxide for 20 minutes, with a GeH_4 flow rates of 40 and 20 sccm, valence band edge was measured as 1.95 eV and 2.41 eV, respectively Increase in valence band edge with increasing N concentration can be explained in the same way as was explained for the increase in energy gap.

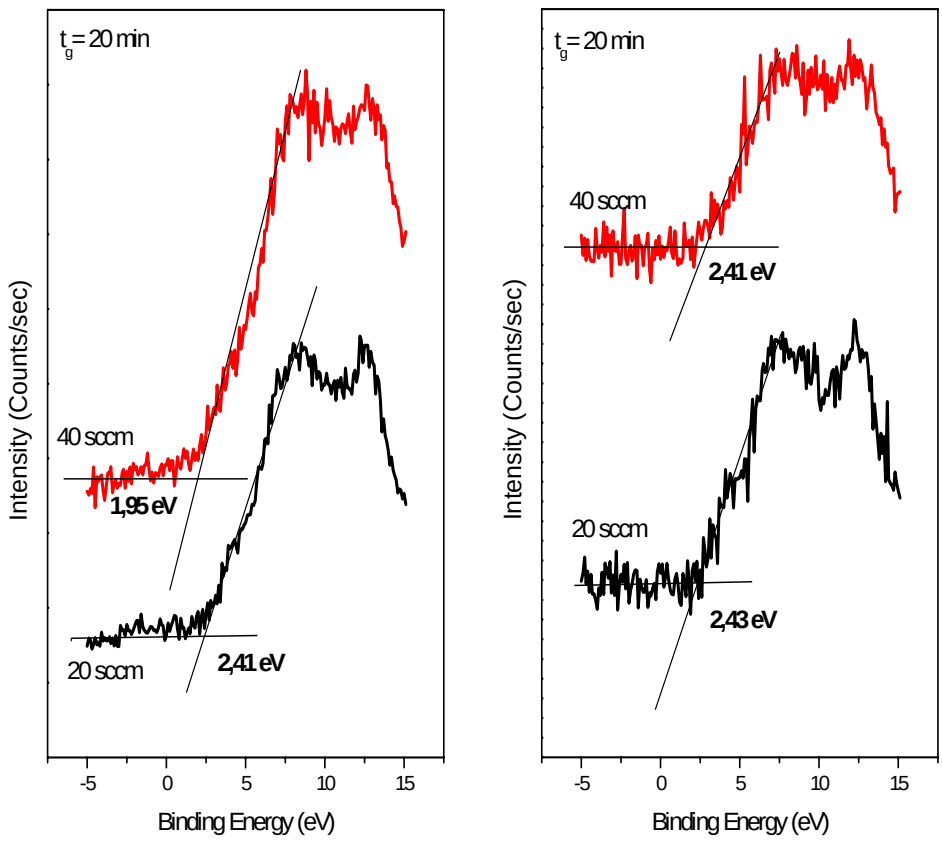

(a) (b)

Figure 3.5.2: Valence band energy spectrum of $Ge_{1-x}N_x$ thin films having 20 sccm and 40 sccm flow rate of GeH_4 with NH_3 flow rate of 50 sccm deposited for 20 min on SiO_2 (a) and Si (b) substrates.

For the samples grown directly on silicon, valence band edge was measured as 2.41 eV and 2.43 eV for 20 and 40 sccm, respectively. The valence band edge of

the samples grown on thermal oxide is greater than those grown on silicon. We suggest that when thickness of the thermal oxide increases valence band edge increases due to photon induced charging effect [28].

Also the valence band edge of the SiO_2 and Si was measured and found as 4.6 eV and 0.37 eV, respectively (Figure 3.5.4). These values are very close to measured ones in the literature [4-25].

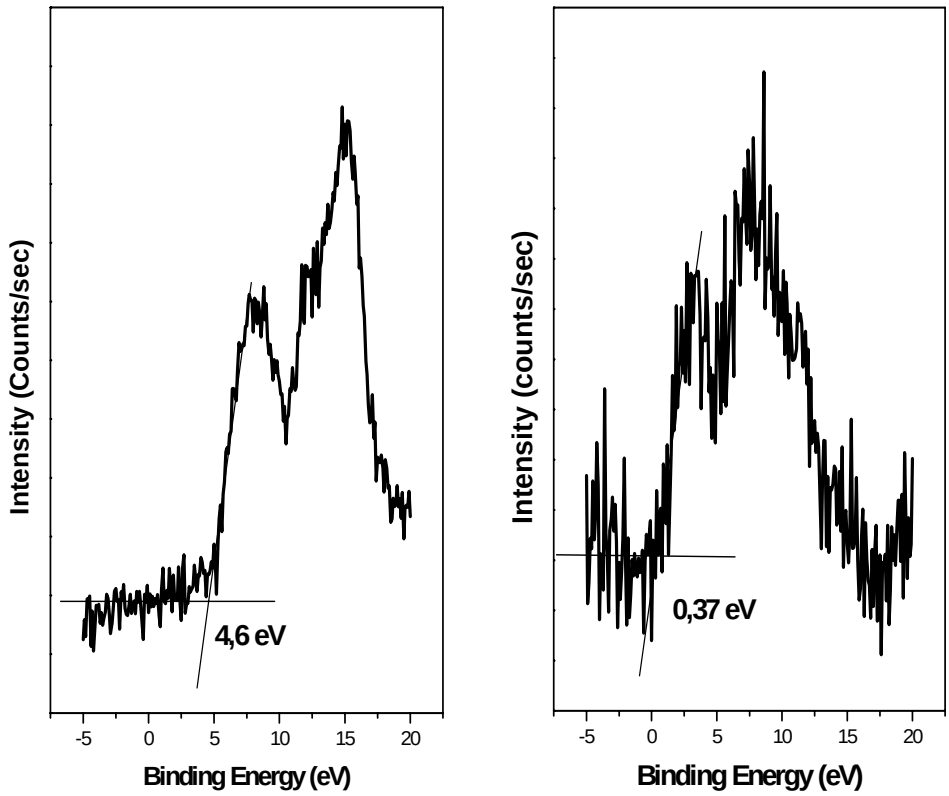

(a) (b)

Figure 3.5.3: Valence band energy spectrum of SiO_2 (a) and Si (b)

Binding energy of the core level can also measured by using XPS. If core level energy, valence band edge and energy gap of the samples are known, valence band

offsets can be calculated for a heterojunction and Schottky diode structures [29]. Valence band offsets can be obtained from the equation [30];

$$\Delta E_V = \Delta E_{CL} + \left(E_{2p}^{A} - E_{VB}^{A}\right) - \left(E_{3d}^{GeN_x} - E_{VB}^{GeN_x}\right) \qquad 3.5.1$$

where

$$\Delta E_{CL} = E_{3d}^{GeN_x} - E_{2p}^{A} \qquad 3.5.2$$

The index of A can be Si or SiO_2 depending on the substrate.

ΔE_{CL} is the core level electron energy difference measured from the heterojunction sample and the other two terms in equation 3.5.1 are the core level energy differences measured from the bulk samples. Conduction band offsets can also be calculated from the differences between energy gaps and valence band offsets values as [24];

$$\Delta E_V = E_{gap}^{GeN_x} - \Delta E_V^{GeN_x - A} - E_{gap}^{A} \qquad 3.5.3$$

Calculated valence band and conduction band offsets values of $SiO_2/Ge_{1-x}N_x$ and $Si/Ge_{1-x}N_x$ structures are tabulated in Table 3.5.1 and 3.5.2 and energy gap values of Si and SiO_2 are taken as 1.1 and 8.1 eV, respectively [8].

GeH4 flow rates (sccm)	Valence band offset (eV)	Conduction band offsets (eV)
20 sccm	2,19	2,19
40 sccm	2,65	2.45

Table 3.5.1: Calculated valence band and conduction band offsets for $Ge_{1-x}N_x$ thin films deposited on SiO_2 for different flow rates of GeH_4.

GeH4 flow rates (sccm)	Valence band offset (eV)	Conduction band offsets (eV)
20 sccm	2,11	1,57
40 sccm	2,29	1,18

Table 3.5.2: Calculated valence band and conduction band offsets for $Ge_{1-x}N_x$ thin films deposited on Si for different flow rates of GeH_4.

The valence band maximum of the systems was estimated using baseline fit method. We found that the valence band offsets at the SiO_2/ $Ge_{1-x}N_x$ interface are 2.19 eV and 2.65 eV for 20 sccm and 40 sccm flow rates of GeH_4, respectively. For the Si/ $Ge_{1-x}N_x$ interface are 2.11 eV and 2.29 eV for 20 sccm and 40 sccm flow rates of GeH_4, respectively.

The differences between samples, grown with different GeH_4 flow rates, while relatively small can most likely be explained with oxygen contamination of the samples during the period between unloading the samples from the PECVD chamber and loading to the XPS vacuum system despite all effort to minimize it. The measurements in this work can therefore be considered preliminary and could be refined further in future work where oxygen contamination is totally avoided. We currently lack the means to do this. In any case, the band offset values obtained in this study suggest that a thin layer of $Ge_{1-x}N_x$ may be useful tool to imrove hole injection into the electronic states of the Si NC Si embedded in SiO_2 in NC based LEDs.

CHAPTER 4: Characterization of $Si_{1-x}Ge_x$ Nanocrystals

4.1. Ellipsometric Characterization

Ellipsometric characterization of $Si_{1-x}Ge_x$ nanocrystals has been done with optical ellipsometry. Tauc-Lorentz model was used to characterize the index of the samples. By considering the material as a mixture of a matrix and nanocrystals, effective medium approximation (EMA) was used for ellipsometric data analysis. Cauchy equation was used with EMA model to describe the refractive index of the film changing with wavelength [31].

$$n(\lambda) = A + \frac{B}{\lambda^2} + \frac{C}{\lambda^4} \qquad 4.1.1$$

For data analyses, thickness of the film layers, A and B constants of Cauchy equation were taken as fitting parameters.

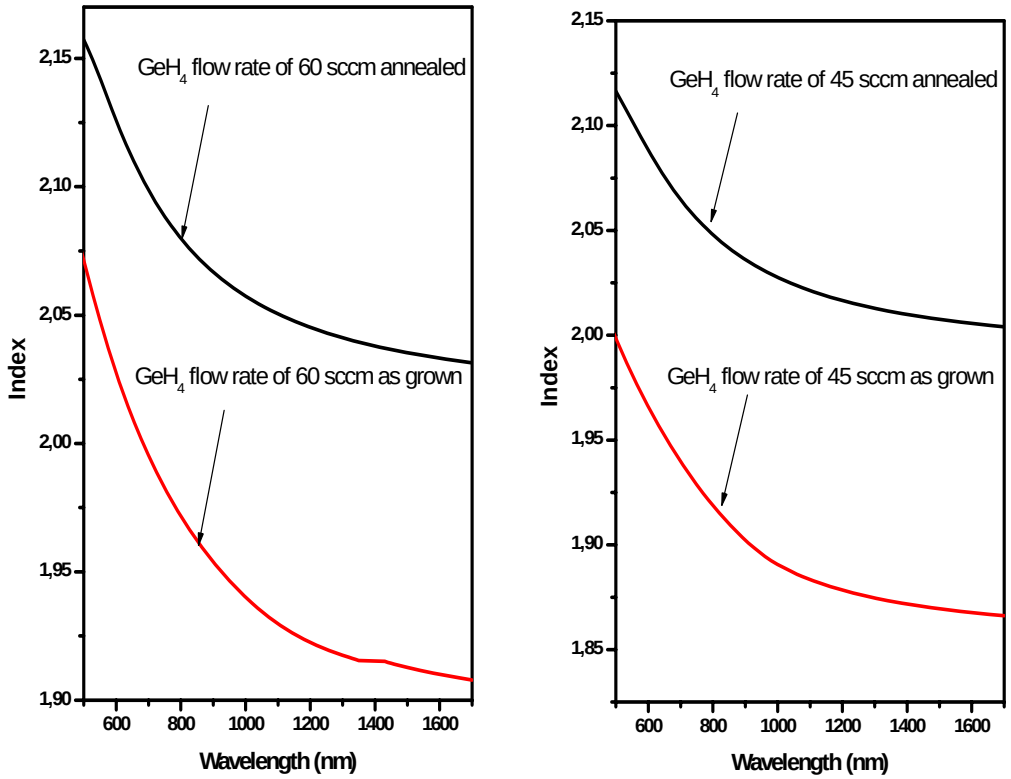

(a) (b)

Figure 4.1.1. The refractive index of the as grown and annealed (1200 ^{o}C for 30 min) Si_xGe_{1-x} films as a function of wavelength for samples having flow rates of 60 sccm (a) and 45 sccm (b) GeH_4.

Figure 4.1.1 shows examples of wavelength dependence of the refractive index of the as-grown and annealed type 3 samples. In accordance with the Cauchy equation, the refractive index increases as the wavelength decreases. This is typical for dielectrics. Furthermore, when the samples are annealed the refractive index increases. This suggests phase separation and the formation of nanocrystals.

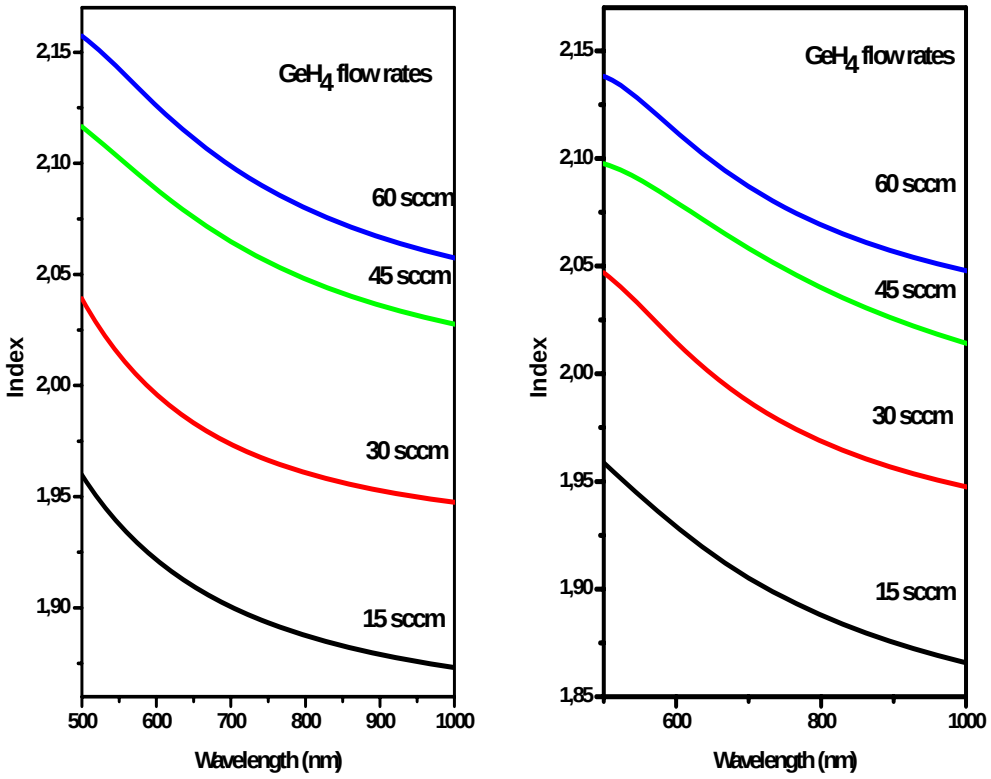

(a) (b)

Figure 4.1.2 Change in index of the Si_xGe_{1-x} nanocrystals as a function of wavelength for various flow rates of GeH_4 annealed at 1200 ^oC (a) and 1100 ^oC (b) for 30 min.

The wavelength dependence of refractive index for samples having different flow rates of GeH_4 annealed at 1200 ^oC and 1100 ^oC for 30 minutes is shown in Figure 4.1.2. As seen from the Figure when Ge concentration inceases, index of the refraction increases. Keeping in mind that these films contain both excess Si and Ge, increasing refractive index with both annealing and GeH_4 flow rate suggests phase separation and therefore, formation of nanocrystals [32].

4.2. Raman Spectroscopy Characterization

4.2.1 Introduction

Raman spectroscopy is widely used technique to analyze materials. Raman spectroscopy is a vibrational spectroscopy technique like Infrared (IR) spectroscopy. IR spectroscopy can be used to identify composition of samples which have a net dipole moment whereas Raman spectroscopy arises from a change in polarizability of the sample. Spectroscopic Raman analyses provide information about electronic properties and lattice dynamics which include identification of materials and compounds, layer orientation, stress and composition.

In this study, Raman spectrometry was used to identify the presence $Si_{1-x}Ge_x$ nanocrystals.

4.2.2 Principles of Raman Scattering

Raman scattering is the inelastic scattering of incident photons from solids. Incident photons that interact with the molecules can be absorbed by the molecules and can be scattered. If these scattered photons have the same energy as the incident photons, this process is called Rayleigh scattering. Energy may also be gained or lost during the scattering process. Changes in the energy of the scattered photon result in shifting of the photon frequency with respect to the incident photon. When the incident photon loses energy by raising the molecules to a vibrationally excited state, this is called as Stokes shifted scattering. When molecules are already in vibrationally excited states, the photon may be scattered with higher energy than the incident photon leaving the molecule in ground state. This process is called as anti-Stokes shifted scatter (Figure 4.2.1).

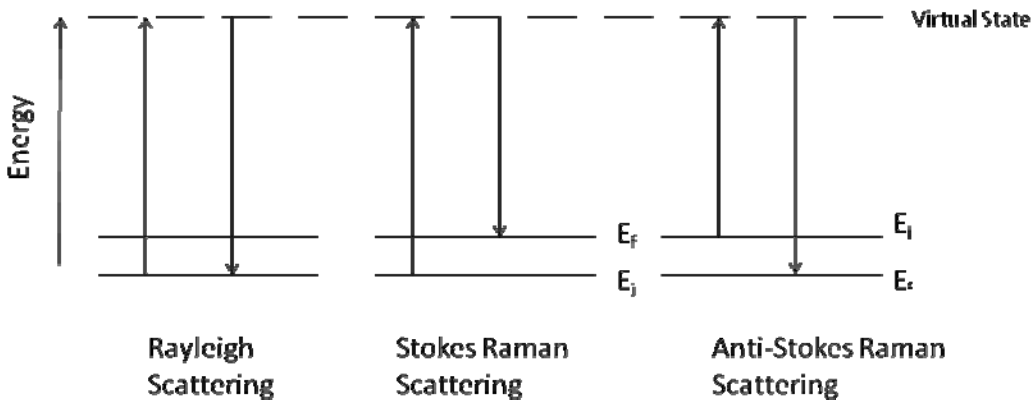

Figure 4.2.1 Energy level diagrams of Rayleigh scattering, Stokes Raman scattering and anti-Stokes Raman scattering.

In solids, optical phonons close to zone centre (k~0) are responsible for the Raman scattering. k~0 selection rule is acceptable for the infinite periodicity of the crystal lattice [33]. When periodicity of the crystal is broken this selection rule is also relaxed. This will be further mentioned in the phonon confinement effect section.

The first order Raman scattering spectra of both bulk Si and bulk Ge contains only one peak. The optical phonon line for Si is at 520 cm^{-1}, whereas the same line is at 300 cm^{-1} for Ge. Alloying Si and Ge results in new peaks and shifting of the parent peaks. Most notably the new peak at 400 cm^{-1} is a clear signature of the formation of SiGe. Also, a weak separate peak due to local vibrational mode of silicon will become observable below 520 cm^{-1}, the exact position depending on various parameters.

However, unlike the bulk SiGe crystals, nanocrystalline SiGe presents further complications in its Raman spectra. While studying the Raman spectra of nanocrystalline $Si_{1-x}Ge_x$, one must consider the effects of several processes such as: phonon confinement, composition and strain on the Raman peaks. The extremely small size of the crystallites results in confinement of phonons in the crystal which effectively results in a frequency shift of the related peak [33]. Furthermore, SiGe is

an alloy which may form with very different compositions. The number of Si and Ge atoms in the nanocrystal will determine its composition. It is well known that frequency positions of the Raman peaks of the alloy will change as a function of alloy composition [34]. Finally, the role of strain in Raman spectroscopy can not outright be neglected [34]. Presence of strain in solids will typically result in frequency shifting of the Raman lines as well the sign of which will depend whether it is tensile or compressive. In what follows, we will try to determine the concentration of samples from the relative intensities and peak positions of Ge-Ge, Si-Ge and Si-Si vibrational modes.

Phonon confinement effect

In an ideal single crystal only optical phonons close to zone centre can be observed with Raman Spectroscopy. For systems having nanoparticles that do not support the vibrational wavenumbers of the material, all phonons can be confined within the nanoparticles of the material. k~0 selection rules mentioned in theory of the Raman scattering is relaxed when periodicity of the crystal is broken. Absence of the periodicity relaxes the selection rule so that phonons away from the Brillouin zone centre can contribute the Raman spectrum as well. This contribution to the Raman spectrum results in asymmetric broadening of the line shape. For a nanoparticle which has finite size, phonon wave function decays close to the particle boundary. This leads to discrete values of wave vector k and its multiples.

For nanoparticles embedded in a host matrix, the phonon confinement can be described as follows: If the optical phonon dispersion curve of the particle does not overlap with that of the host matrix, propagation of the phonons seems to be impossible and they become confined in the nanocrystals.

Several models have been used to investigate optical phonon confinement in nanocrystals. These methods are Gaussian Confinement Model (GCM), Continuum Theory and Microscopic Lattice Dynamical Calculations [33]. Most commonly used model for nanoparticles is the Gaussian Confinement Model proposed by Richter et al [35] and generalized by Campbell and Fauchet [36]. This model is based on the contributions of the phonons away from the zone centre. To describe

this model, consider a spherical nanoparticle of diameter of D and phonon wave function Ψ (q_o, r). This wave function must be multiplied by envelope function W(r) which decays close to zone centre, because of the existence of the phonon wave function within the particle. Plane-like wave function can not propagate beyond the crystal surface. Envelope function is commonly chosen as a Gaussian function as;

$$W(r,L) = \exp\left(\frac{-\alpha r^2}{L^2}\right) \qquad 4.2.1$$

where α is related with how rapidly wave function decays.

One-photon Raman scattering weight function C(q) which is used to define the contribution of the phonons away from zone edge and which is simply Fourier transform of the envelope function is [33].

$$C(q_o,q) = \frac{1}{(2\pi)^3}\int d^3q\,\Psi(q_o,r)e^{-iq.r} \qquad 4.2.2$$

Using these functions, first order Raman Spectrum is obtained by integration as

$$I(\omega,L) \approx \int d^3q\,\frac{|C(q,L)|^2}{[\omega-\omega(q)^2]^2+(\gamma_o/2)^2} \qquad 4.2.3$$

where ω(q) is phonon dispersion relationship and γ_o is the natural line width of the optical phonon for bulk materials.

Both Si and Ge have exact phonon dispersion relationships. However, no optical dispersion relation has been reported for SiGe bulk or nanocrystals [34]. This makes the exact evaluation of the equation for the line shape spectrum impossible. One needs to consider either the Si or the Ge bulk dispersion curves which is an over simplification. Phonon confinement effect of nanoparticles such as Si and Ge

has been studied by several researchers. H. Richter et al. studied the phonon confinement effect starting with c-Si for the stress free samples. They used oxidation techniques to form Si nanocrystals from bulk Si samples. They found linewidths as large as γ=51 cm^{-1}, frequency shifts $\Delta\omega$=16 cm^{-1} and they have taken α as $8\pi^2$. They have shown that linewidths of the Si-Si mode increases with decreasing annealing temperature [35]. Making use of the phonon confinement and using porous SiGe samples, the $Si_{1-x}Ge_x$ nanocrystals sizes were estimated to be 12.0 nm, 16.1 nm and 19.3 nm, with decreasing posity by Kartopu et al. [37]. They assume that that their nanocrystals are stress free and their composition is well known.

Effect of strain and concentration

In the study of SiGe nanocrystals in SiO_2 matrix, one must also consider the the effect of strain, as well. Different elastic constants of the nanocrystals and that of the surrounding medium, coupled with high temperature annealing, may result in tensile stress. Compressive stress may result due to mismatch between nearest neighbour distance [38] or volume expansion upon solidification [39]. Compressive stress results in blue shifting of the Raman line while phonon confinement results in red shifting of the Raman line. Both the magnitude for the stress as well as phonon confinement is expected to be effected by the composition of the SiGe nanocrystals. Finally, natural Ge is composed of several isotopes. Considering that the Raman shifts between the lightest and the heaviest isotopes of Ge which is 12.5 cm^{-1} [40]. The effect of isotopic distribution of Ge in the matrix may contribute significantly to the Raman peak position. In the absence of any information on the GeH_4, we assume the peak position of natural Ge as 305 cm^{-1} [40].

Considering the effects of phonon confinement, stress and composition we refrain from attempting an analysis of the Raman line shift and its connection to nanocrystals size. The uncertaininties associated with these effects are further complicated with the weighing functions employed in such an analysis, whether Gaussian or sinc like .

Although phonon energies depend on both concentration and strain, intensities of these modes depend only on concentration. The relative intensity ratios of Si-Si, Si-Ge and Ge-Ge are related with concentration as $(1-x)^2$, $2x(1-x)$ and x^2, respectively. (40). The exact dependence of concentration, frequency and relative intensity of the peaks can be given by;

$$\frac{I_{Si-Si}}{I_{Ge-Ge}} = \frac{n_{Si}}{n_{Ge}} \frac{\omega_{Ge-Ge}}{\omega_{Si-Si}} \frac{x^2}{(1-x)^2} \qquad 4.2.4$$

Here the ratio of the intensity of Si-Si mode to that of the Ge-Ge is given in terms of the phonon occupation numbers for Si and Ge indicating the relative strengths of the said lines as well as the Raman frequencies and composition, x. By measuring samples under similar conditions, composition of the SiGe nanocrystals can be calculated. We have done this analysis to extract the composition of the SiGe nanocrystals.

4.2.3 Experimental setup

Raman measurements were taken on a double monochromotor at room temperature with the 488.0 nm line of Argon laser at power of 300 mW to determine the presence of $Si_{1-x}Ge_x$ nanocrystals in the samples. First stage of the monochamotor (Figure 4.2.2) used in this experiment has one entrance slit to collect light, two mirrors used to collimate light onto and out of the grating to an exit slit. The two monochromators are serially connected to improve resolution at the cost of reduced throughput. Light passing through the final exit slit is detected by the CCD or photomultiplier which are light detectors providing a current output proportional to light intensity. For most of the work presented in this work, several lines of an argon ion laser were used, most notably at 488.0 nm and 514.5 nm. Laser light was focused onto the samples using a cylindrical lens to minimize laser induced changes or damage to the samples while F# matched optics was used to collect and focus the scattered to the entrance slit of the monochromator.

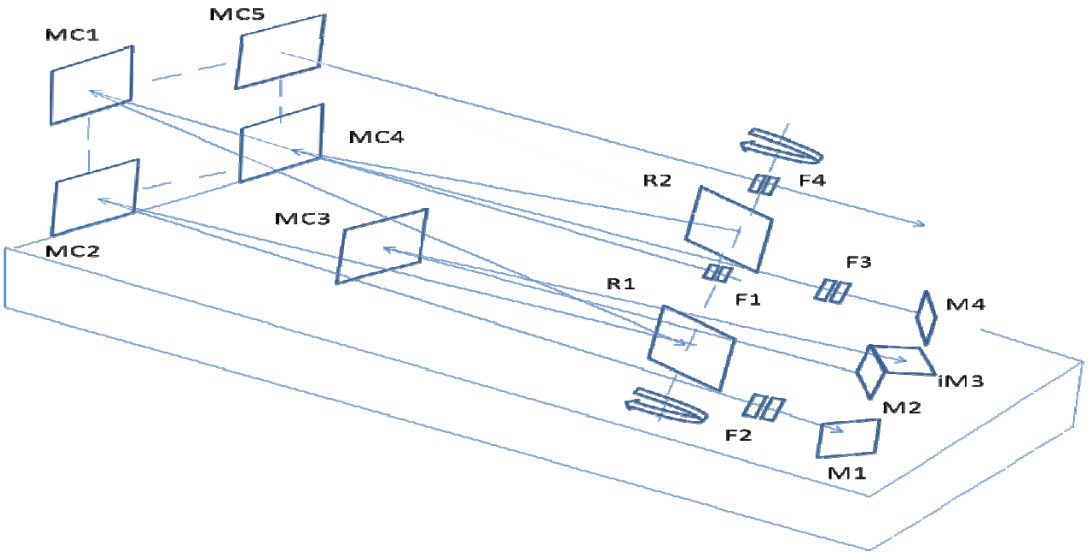

Figure 4.2.2 Detailed layout of the double monochromator used in the experiment

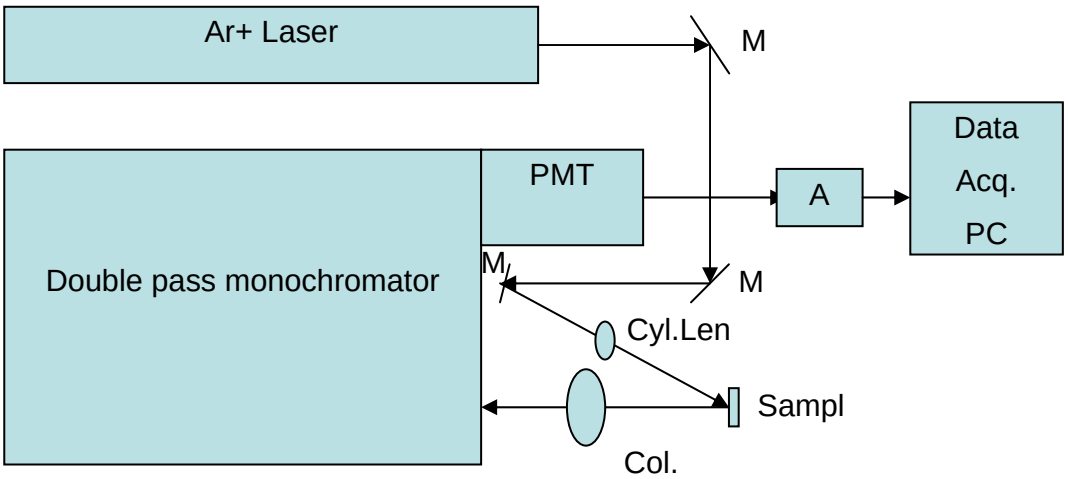

Fig. 4.2.3. Experimental setup used in the Raman experiments

4.2.4 Raman Spectrum Analyses of $Si_{1-x}Ge_x$ Nanocrystals

Several approached were tried to form the SiGe nanocrystals. In the first of these, a series of samples have been deposited with different thicknesses of thin a-Ge and a-Si layers in between SiO_2 layers (Sample Type1 and Sample Type 2 as described in Chapter 2) and annealed at different temperatures. Both a-Si and a-Ge layers mix and precipitate into crystallites in the amorphous SiO_2 matrix upon annealing. To demonstrate the effect of annealing temperatures, Raman spectrum of these films grown on silicon substrates annealed at various temperatures under various atmospheres were studied and shown in Figure 4.2.4.

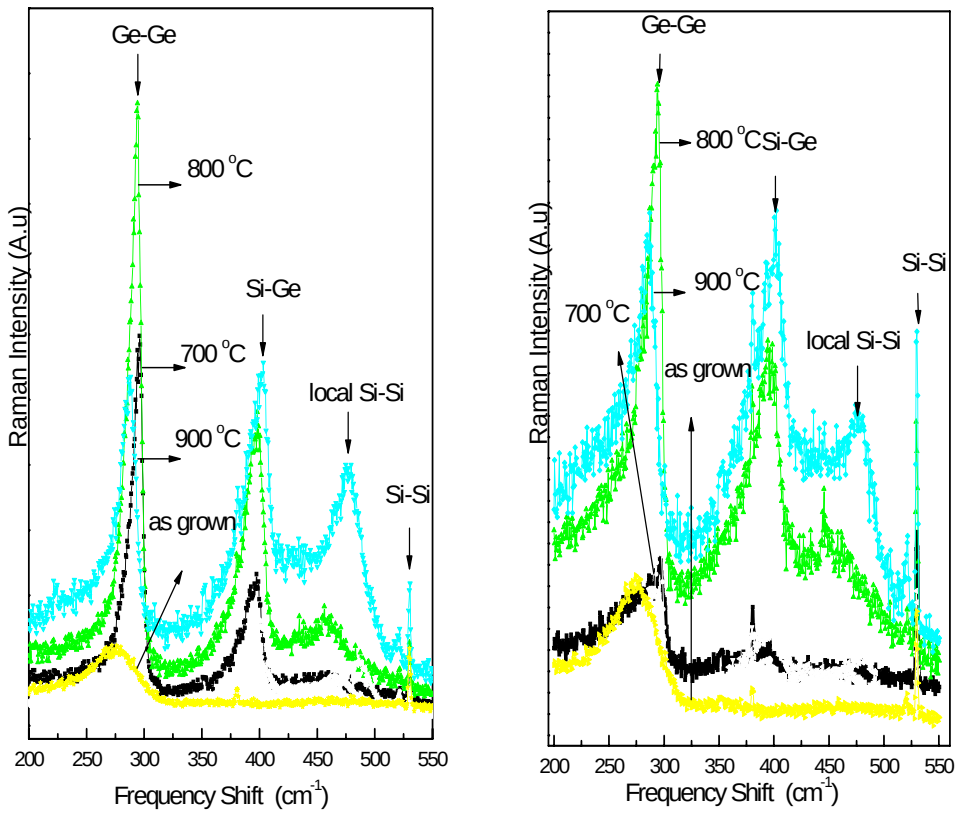

(a) (b)

Figure 4.2.4. Raman spectra of $Si_{1-x}Ge_x$ NC's sample 1 (a) and sample (2) annealed at various temperatures for 7.5 min.

As shown in the Figure 4.2.4 as grown samples show a broad peak centered around 275 cm^{-1} and a peak at 520 cm^{-1}. The broad peak corresponds to quasi amorphous Ge in the samples while the sharp peak at 520 cm^{-1} corresponds to Si substrate. Once annelead, the spectra changes completely. Several prominent peaks are observed around 295 cm^{-1}, 400 cm^{-1},485 cm^{-1} and 521 cm^{-1}. These peaks are assigned to the Ge-Ge, Si-Ge, Si-Si local and Si-Si vibration modes, respectively [3]. At 700 ^{o}C the Ge-Ge related peak shifts up to 290 cm^{-1} indicating the onset of crystallization of Ge layer. As the annealing temperature rises even higher, the Ge-Ge vibration mode sharpens up and shifts to higher wavenumbers. This is accompanied by the strengthening of the Si-Ge mode which also moves to higher wavenumbers. Considering the broad nature of all the modes, it is expected that the SiGe nanocrystals in these samples are very small.

While formation of SiGe is clearly monitored by Raman spectroscopy, continous nature of the as deposited a-Si and a-Ge layers sandwiched between SiO_2 layers make nanocrytalline nature of these samples suspect. In order to clarify this point we have studied TEM data from selected samples.

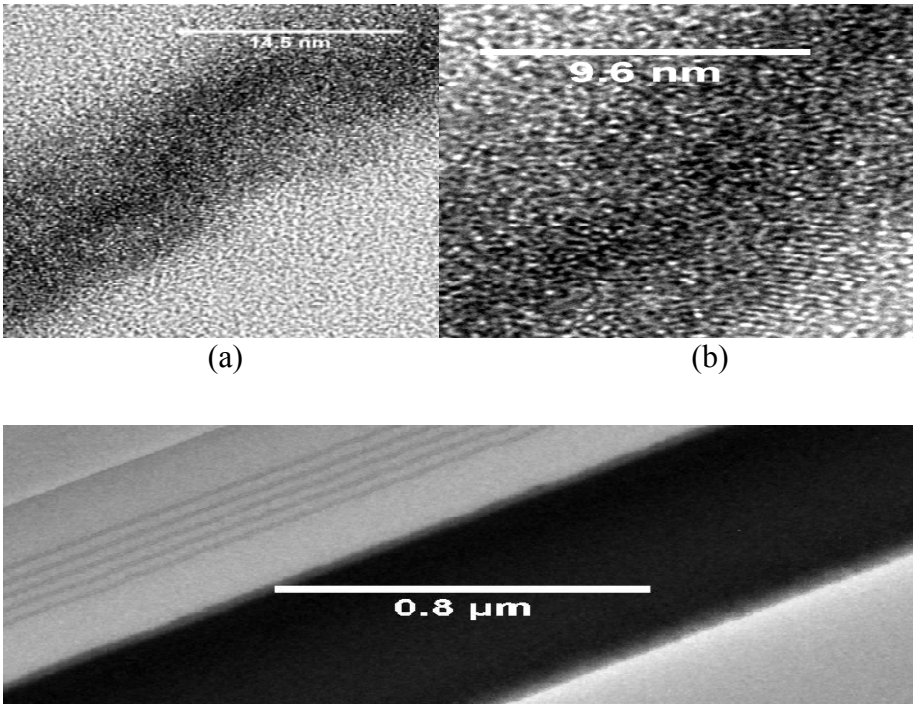

(a) (b)

(c)

Figure 4.2.5 TEM images of the Sample 1 and Sample 2 $Si_{1-x}Ge_x$ NC. (Thanks to FEI)

Figure 4.2.5 shows the transmission electron spectrum (TEM) images for the samples 1 and 2. Multilayer features of the sample are clearly delineated in the figure (c). The SiGe layers are well defined and are in straight lines seperated by the intervening oxide layer. Figure 4.2.5 (a) and (b) show a single layer of the sample at high magnification. A continuous band of high contrast material indicating that the SiGe layer is composed of continuous layer of quasi -amorphous material laden with small crystallites. With the objective of obtaining discrete nanocrystals in mind as our objective we, therefore, decided to try different approaches for the formation of the SiGe nanocrystals.

Alternatively, both Si and Ge were mixed in during the growth of the oxide layer (Sample Type-3). Raman spectrum of the films grown on silicon substrate with

fixed amount of excess Si but with variable Ge concentration was studied. These samples were single layers, and contained both a fixed amount of excess Si and varying amounts of excess Ge. Furthermore, in order to eliminate the possibility of oxidation, these samples were annealed in N_2 environment. Raman spectra of a single layer samples grown on silicon annealed at temperatures 1200 ^oC for 1100 ^oC for various times. These samples were grown with various GeH_4 flow rates. For the samples with GeH_4 flow rate of 30 sccm, 45 sccm, and 60 sccm, several prominent peaks were observed around 305 cm^{-1}, 400 cm^{-1}, 476 cm^{-1} and 521 cm^{-1}. These peaks are assigned to Ge-Ge, Si-Ge, local Si-Si and crystalline Si-Si vibrational modes, respectively [3]. The peak at around 400 cm^{-1} is the signature for SiGe formation. Only when the flow rates of GeH_4 are fixed at 30 sccm (Figure 4.2.6), 45 sccm (Figure 4.2.7), and 60 sccm (Figure 4.2.8), Si-Ge mode is observed. We do not observe SiGe modes for samples grown with 90 and 120 sccm GeH_4 flow rates. This means that formation of SiGe nanocrystals is easier at lower Ge concentrations mostly likely because the amount of Ge is too high and dominates the material.

The general character of all the Raman spectra remains the same with respect to the peaks present depending on the annealing temperature and duration as well as on the GeH_4 flow rate. Due to higher diffusion coefficients, higher temperatures and due to longer diffusion times (and therefore lengths), longer anneal times may be expected to produce shifts on the peaks.

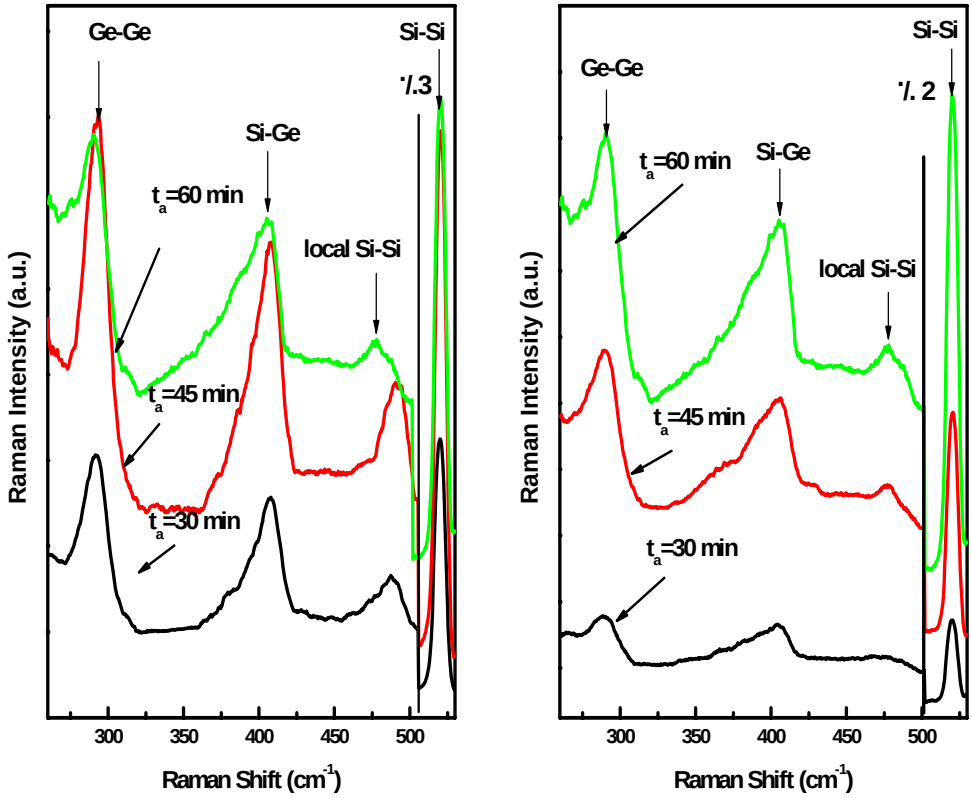

(a) (b)

Figure 4.2.6:Raman spectra of $Si_{1-x}Ge_x$ NC's samples having 30 sccm flow rates of GeH_4 annealed at 1200 ^oC (a) and 1100 ^oC (b) for various time.

Optic phonon mode of the unstrained bulk Ge is at 302 cm^{-1} (11). Shift of Ge-Ge modes from its bulk position to lower or higher wave numbers may be related with phonon confinement, strain and also composition. With increasing Ge concentration Ge-Ge mode (Table 4.2.2) shifts to higher wave numbers [41]. The linewidths that we measure for Ge-Ge mode of $Si_{1-x}Ge_x$ nanocrytals from the Raman spectra are of the order of 17 cm^{-1}. Compare with the linewidth of 5 cm^{-1} of the Ge-Ge modes in bulk Ge [40]. This linewidth becomes asymmetric and broader with decreasing Ge concentration due to random distributions in the alloy, disorders and defects [42-43]. Peculiarly, we do not observe Si-Ge mode in samples with the highest concentrations of Ge and Ge-Ge mode intensities are higher in samples with lower concentration. This suggests that the amount of Si in these nanocrystals is no longer sufficient to produce SiGe alloy and the system is dominated by Ge.

The local Si-Si peak is present only in samples with relatively low Ge concentrations and is not seen in samples with higher Ge concentrations. Frequency of Si-Si local vibrational mode is sensitive to Ge content [3]. The frequency of Si-Si peaks decreases with bonding of one or more Ge atoms to Si from 520 cm^{-1} to 486 cm^{-1} down to 450 cm^{-1}.The Si-Si phonon mode shows a red shift with increasing Ge content and the intensity of the Si-Si decreases with increasing Ge concentration [44-45]. This is because of the increase in bonding atom mass.

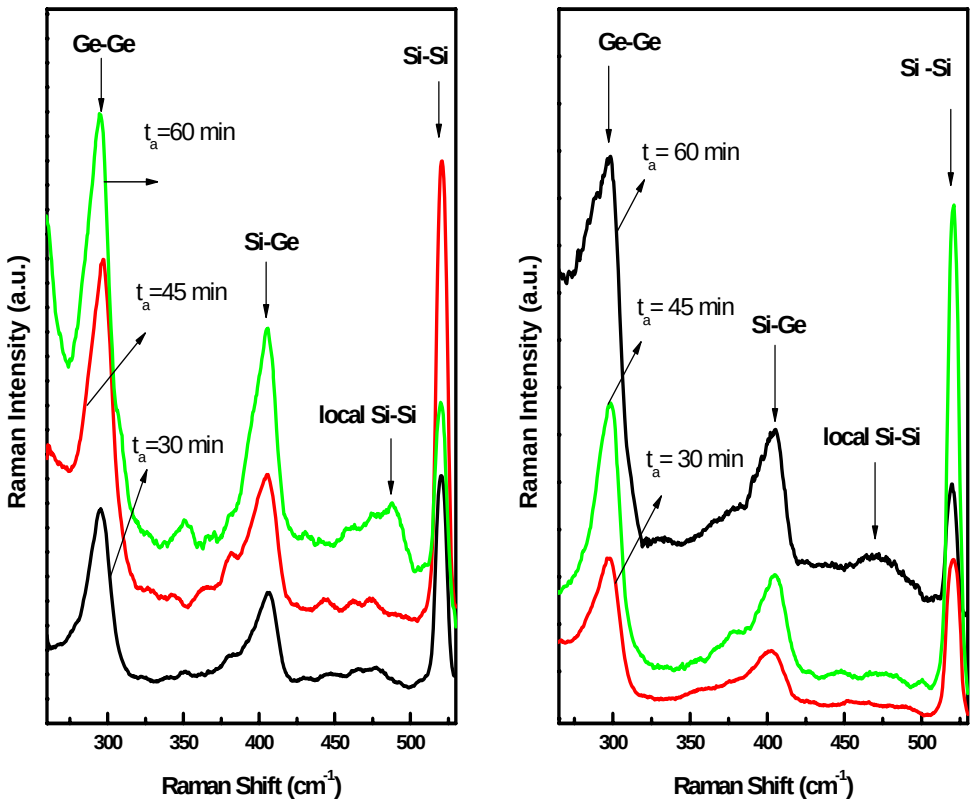

(a) (b)

Figure 4.2.7. Raman spectra of SiGe NC's samples having 45 sccm flow rates of GeH_4 annealed at 1200 ^oC (a) and 1100 ^oC (b) for various times.

In order to confirm the data presented above, we repeated the same experiments on samples annealed for various times. Basic features of the data are the same for different annealing times. Si-Si peaks evolve as Ge concentration decreases as was

shown in all Raman spectra. The position of the Si-Ge mode shifts to the lower frequency with increasing annealing time due to relaxation of strain [42]. Also, local Si-Si peak shifts shows that annealing decreases to strain in the Si layer [43] and intensity of the Si-Si peak decreases with increasing annealing time. With increasing annealing time FHMW of Ge-Ge and Si-Si modes decreases faster than that of Si-Ge. This is because weak features become significant at low annealing temperatures [34]

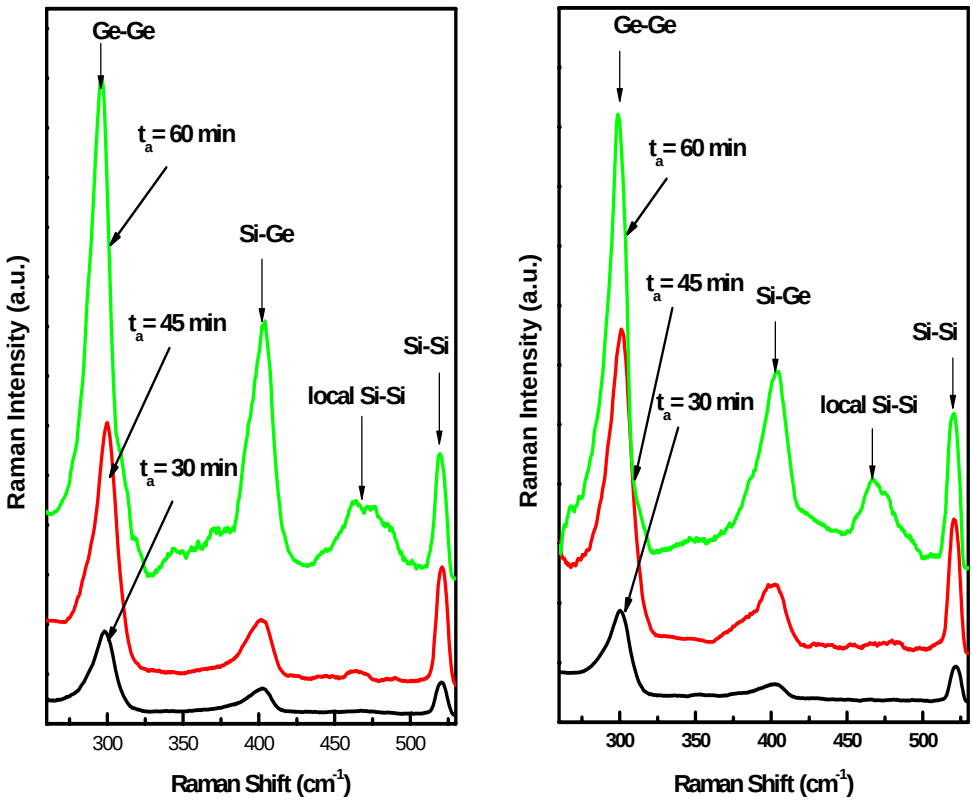

(a) (b)

Figure 4.2.8. Raman spectra of SiGe NC's samples having 60 sccm flow rates of GeH_4 annealed at 1200 ^oC (a) and 1100 ^oC (b) for various times.

We summarize the peak positions of all the samples in the following tables.

GeH_4 flow rates	Annealing time and temperature (C, min)					
	1200-30	1200-45	1200-60	1100-30	1100-45	1100-60
30 sccm	404,2	404,8	395,4	397,6	401,3	397,2
45 sccm	403,5	401,7	403,5	402,8	400,0	399,5
60 sccm	399,9	399,6	401,7	399,1	398,2	401,3

Table 4.2.1 : Si-Ge modes in the Raman spectra of SiGe nanaocrystals in cm^{-1}

GeH_4 flow rates	Annealing time and temperature (C, min)					
C-min.	1200-30	1200-45	1200-60	1100-30	1100-45	1100-60
30 sccm	291,8	292,8	290,7	289,8	289,8	290,4
45 sccm	294,6	295,8	295,7	296,0	296,5	294,9
60 sccm	297,5	298,9	296,1	299,4	300,2	298,5

Table 4.2.2 : Ge-Ge modes in the Raman spectra of SiGe nanaocrystals in cm^{-1}

GeH_4 flow rates	Annealing time and temperature (C, min)					
C-min.	1200-30	1200-45	1200-60	1100-30	1100-45	1100-60
30 sccm	485.6	489.1	480.5	475.0	478.1	480.4
45 sccm	476.1	471.7	479.2	472.7	477.3	474.3
60 sccm	470.8	470.4	472.1	470.1	475.8	470.0

Table 4.2.3 : Si-Si local modes in the Raman spectra of SiGe nanaocrystals in cm^{-1}

We first perform the intensity analysis using equation 4.2.4. For the intensities of Si-Si and Ge-Ge modes we use integrated area intensities. Phonon occupation numbers for Si and Ge were calculated at room temperature. We note that equation 4.2.4 is independent of assumptions regarding phonon confinement and stress. The values calculated from equation 4.2.4 are summarizing in the table below.

GeH_4 flow rates	Annealing time and temperature				(C, min)	
	1200-30	1200-45	1200-60	1100-30	1100-45	1100-60
$Si_{1-x}Ge_x$	x	x	x	x	x	x
30 sccm	0,51	0,50	0.55	0,61	0,59	0,55
45 sccm	0,58	0,62	0,61	0,63	0,61	0,56
60 sccm	0,55	0,56	0,64	0,56	0,59	0,60

Table 4.2.4: Ge concentration of $Si_{1-x}Ge_x$ nanocrystals.

From Table 4.2.4 we note that in general the concentration of Ge is around 55% for a given annealing time and temperature. There is a negligible decrease with increasing annealing time and temperatures.

As GeH_4 flow rate is increased Si-Ge modes sharpen up and shift towards higher wavenumbers (Table 4.2.1). The shift of phononic energy shift in nanocrystals may in general, depend on phonon confinement, composition and strain effects. As the nanocrystal size decreases, the Si-Ge mode is expected to shift to lower wavenumbers due to confinement of optic phonons in SiGe nanocrystals of several nanometer sizes. The Si-Ge vibrational energies exhibit only weak compositional dependence but its line width and intensities [37] depend on composition. The assymmetry of the Si-Ge modes increases with Ge concentration indicating that linewidth of the Si-Ge mode is determined by nanocrystal composition [46]. It is well known that even in bulk semiconductor alloys have broader Raman lines than their parent systems, due to what is known as alloy fluctuation. Random

distribution of the atoms in nanocrystals and different sizes of the atoms involved results in broadening of the Raman lines.

We plot the Raman frequency of Ge-Ge mode of the SiGe nanocrytals as a function of anneal time and GeH_4 flow rate in Fig. 4.2.9 for samples annealed at 1100 ^oC and 1200 ^oC. The samples annealed at 1100 ^oC show an increase in the Raman frequency of the Ge-Ge mode as a function of the GeH_4 flow rate. As the flow rate increases from 30 sccm to 60 sccm, there is a shift of approximately 10 cm^{-1}. The change in Raman frequency as a function of anneal time is, however, negligible. Following the arguments made earlier on phonon confinement, one would expect that as the crystal size increases the effect of phonon confinement would weaken. Furthermore, the Raman work on bulk SiGe alloys suggests that [3] Raman frequencies of SiGe mode changes little with alloy composition which makes the use of experimental SiGe mode frequencies not useful [40]. However, from Table 4.2.3. it is possible to determine the Raman frequencies of the Si-Si local modes and using the available data in the literature for bulk SiGe we can determine the composition of our samples. The Raman frequency of the Si-Si local vibrational modes varies from 488 cm^{-1}, 490 cm^{-1} to 477 cm^{-1} for samples grown with 30, 45, 60 sccm, and annealed at 1200 ^oC corresponding to 50, 48, and 60 % Ge while for the same samples annealed at 1100 ^oC we observe 476 cm^{-1}, 477 cm^{-1}, 477 cm^{-1}, corresponding to 60% Ge. The composition analysis obtained from the frequency analysis of the Si-Si mode given above is remarkably consistent with the calculated Ge composition from integrated area intensities of Si-Si and Ge-Ge modes.

From the compositional dependence of Ge-Ge mode [40] we find that the observed Ge-Ge mode frequency is 289 cm^{-1}. The Ge-Ge Raman frequency we observe for these samples grown at 30 sccm and annealed at 1100 ^oC and 1200 ^oC for 30 min is 290-292 cm^{-1}. Considering that phonon confinement effects result in blue shift of the phonon line as opposed to the red shift of the tensile stress effect, a dominating phonon confinement should give us frequencies lower than 289 cm^{-1}. However, this is not observed. On the contrary, we observe a red shift of 3 cm^{-1} which can only be due to strain caused by tensile stress. The amount of red shift due

to strain masks the blue shift due to phonon confinement, however small. The existence and increase of strain in SiGe nanocrystals can be justified considering that introduction of excess Ge, however small, into the SiGe lattice would strain the nanocrystal due to the relatively large size of Ge atom when compared with Si atom.

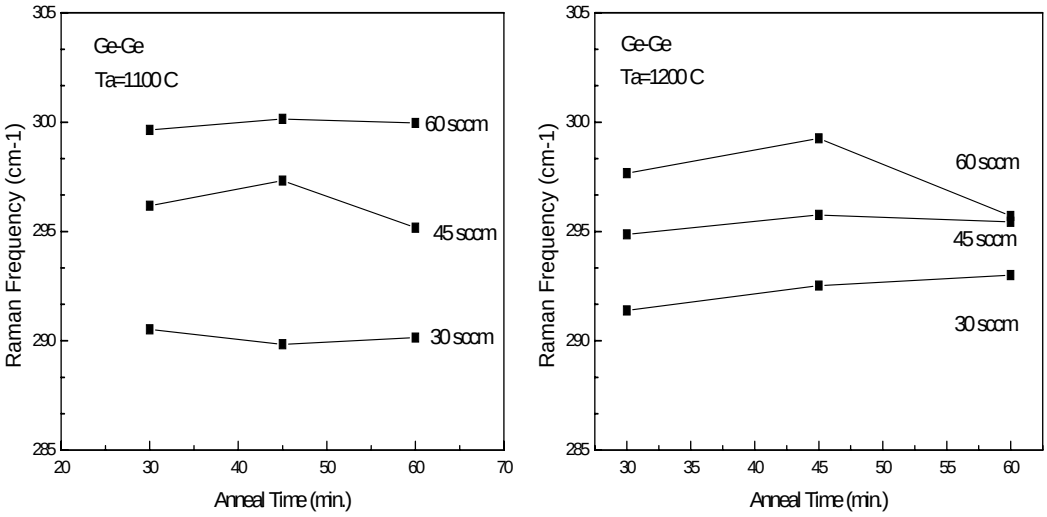

Figure 4.2.9: Raman frequency of Ge-Ge mode of the SiGe nanocrytstals for annealed at 1100 ^{o}C and 1200 ^{o}C as a function of GeH_4 flow rates.

Finally, we present the Raman spectra of samples grown with 90 sccm and 120 sccm flow rates of GeH_4 as shown in figure 4.2.10 for completeness. As was mentioned earlier, we do not observe any sign of a SiGe mode and this is mostly likely due to the fact that the system is dominated by high Ge concentration.

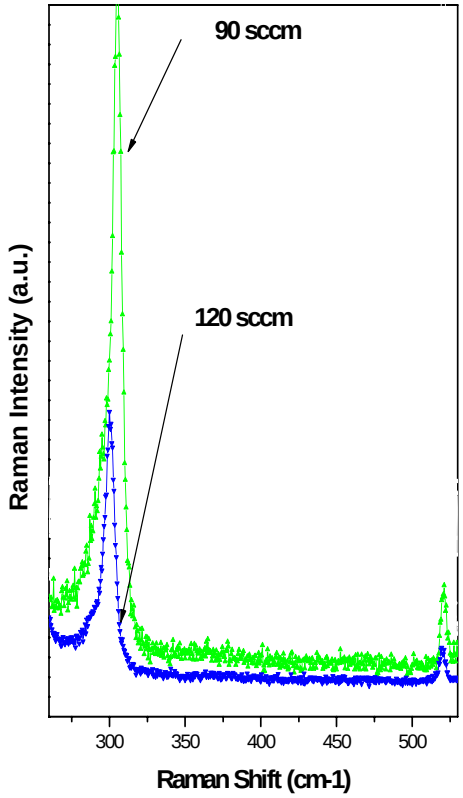

Figure 4.2.10.Raman spectra of SiGe NC's samples having 90 sccm and 120 sccm flow rates of GeH_4 annealed at 1200 ^oC for 30 minutes.

In conclusion, we have been able to prepare SiGe nanocrystals using PECVD and post annealing. We were able to calculate the composition of the nanocrystals and find that they are under strain which is reflected in their Raman spectra.

CHAPTER 5: Conclusions and Future Work

SiGe nanocrystals and $Ge_{1-x}N_x$ thin films formations have been studied via ellipsometry, Raman scattering, FTIR as well as XPS on samples prepared by plasma enhanced chemical vapor deposition technique. $Ge_{1-x}N_x$ films were deposited on silicon (100) wafers, quartz and with 4 nm thermal oxide using PECVD using the gas mixtures of NH_3 and GeH_4. For all samples, the flow rate of NH_3 was fixed at 50 sccm and various flow rates of GeH_4 were performed. $Si_{1-x}Ge_x$ films having different layering order were deposited on silicon (100) wafer as a single layer using gas mixture of SiH_4, N_2O and GeH_4. The flow rates of SiH_4, N_2O were fixed at 220 sccm, 8 sccm, respectively and various flow rates of GeH_4 (120, 90, 60, 45, 30, 15 sccm) were used. Working pressure was maintained at 1000 mTorr and RF power was 12 W. The temperature of the substrates was fixed at 350 ^oC. A range of annealing temperatures and times has been tried under N_2 ambient atmosphere. Optimum processing conditions are determined.

Refractive index of the $Ge_{1-x}N_x$ films measured by optical ellipsometry. We note that index of refraction increases with increasing GeH_4 flow rate. All data obtained are in aggrement with the literature. The FTIR spectrum confirmed the existence of $Ge_{1-x}N_x$ thin films. All as grown and annealed samples have an absorption line at around 730 cm^{-1} in the IR spectrum. This Infrared transmission analysis of the films suggests that films contain both amorphous germanium nitrides. We studied the same $Ge_{1-x}N_x$ films with Raman spectra and samples grown with 20 and 40 sccm both show no peaks. This may be the amorphous structure of the films or transparency of the films to the laser line. However, Raman Spectra shows that, $Ge_{1-x}N_x$ thin films display the crystallization of $Ge_{1-x}N_x$ at higher temperatures which clearly indicates the formation of crystalline germanium due to decomposition of $Ge_{1-x}N_x$ films.

Furthermore, band offsets of these samples determined by XPS via valence band measurements and optical band gap of the films was calculated with transmission spectrum measured by optical ellipsomety. It was shown that optical

band gap of the films changes by changing nitrogen concentration. The valence band maximum of the systems was calculated using baseline fit method. We found that the valence band offsets at the SiO_2/ $Ge_{1-x}N_x$ interface are 2.19 eV and 2.65 eV for 20 sccm and 40 sccm flow rates of GeH_4, respectively. For the Si/ $Ge_{1-x}N_x$ interface are 2.11 eV and 2.29 eV for 20 sccm and 40 sccm flow rates of GeH_4, respectively. Calculated band offsets show that $Ge_{1-x}N_x$ can be suitable for hole injection in light emitting diodes.

The index of the $Si_{1-x}Ge_x$ nanocrytals was measured with ellipsometry. Ge concentration and annealing temperature dependencies have been studied. The result is that, the index of refraction of the nanocrystals increases with increasing annealing temperature and Ge concentration.

Raman spectra of SiGe samples indicate that formation of SiGe structures by PECVD growth and annealing is possible. Typically samples showed Ge-Ge, Si-Ge, nanocrystalline Si-Si local and Si-Si peaks due to the substrate at wavenumbers of approximately 295 cm^{-1}, 400 cm^{-1}, 485 cm^{-1} and 521 cm^{-1}, respectively. Lower concentrations of Ge in the films are better suited for the formation of SiGe modes. Higher Ge concentrations do not show Si-Ge modes. The appearance of the Si-Ge mode is accompanied by the Si-Si mode at around 500 cm^{-1}. This mode is also not observed for samples with higher concentrations of Ge. Increase in Ge concentration, Ge-Ge mode shifts to higher wave numbers and Si-Ge modes sharpen up and shift towards lower wavenumbers.

Furthermore, the change in Raman frequency as a function of anneal time is so small. The observed Ge-Ge mode for low Ge concentration is 290 cm^{-1}. Following the earlier work this suggests that effect of phonon confinement would weaken. When Ge concentration increases, Ge-Ge mode shifts to the higher wavenumbers. This indicates that excess Ge in the lattice of the SiGe nanocrystals causes stress. Furthermore, the Raman work on bulk SiGe alloys suggests that Raman frequencies of SiGe changes little with alloy composition. If the films are assumed to be stress free the Ge concentration of the films was calculated as 50 %-60 %.

REFERENCES

[1] A. R. Zanatta, I. Chambouleyron, "Nitrogen in The Amoprhous-Germanium Network: From High Dilution to The Alloy Phase", Phys. Rev. B, **48(7)**, 4560, (1993).

[2] W. Y. Leong, L. T. Canham, I. M. Young, D. J. Robbins, "Electronic quality of vapour phase epitaxial Si grown at reduced temperature",Thin Solid Films, **184 (1-2),** 131, (1990).

[3] M. I. Alonso, K. Winer, "Raman Spectra of c-$Si_{1-x}Ge_x$ Alloys" Phys. Rev. B, **39(14),** 10056 (1989)

[4] A. M. Goodman, "Photoemission of Holes from Silicon into Silicon Dioxide", Phys. Rev. B, **152**, 780, (1966).

[5] A. Tabata, N. Matsuno, Y. Suzuoki, T. Mizutani, "Optical properties and structure of SiO_2 films prepared by ion-beam sputtering". Thin solid Films, **289 (1-2)**, 84-89, (1996).

[6] A. R. Zanatta, I. Chambouleyron, P.V. santos, "Electronic structure of amorphous germanium-nitrogen alloys: A UV photoelectron spectroscopy study" J. Appl. Phys. , **198-200 (1-2),** 136, (1996)

[7] J. Xu, K. Chen, D. Feng, S. Miyazaki, M. Hirose, Preparation of Hydrogenated Amorphous Germanium Nitrogen Alloys by Plasma Enhanced Chemical Vapor Deposition", J. Appl. Phys., **80 (8)**, 4703, (1996)

[8] A. B. Young, J. J Rosenberg and Szendro I," Preparation of Germanium Nitride Films by Low Pressure Chemical Vapor Deposition", J. Electrochem. Soc., **134 (11),** 2867, (1987).

[9] Min She, Tsu-Jae King " Impact of crystal size and tunnel dielectric on semiconductor nanocrystal memory performance " Electron Devices, IEEE Transactions on. **50 (9),** 1934-40, (2003).

[10] M. Kanoun, A. Souifi, T. Baron, F. Mazen "Electrical study of Ge nanocrystal based metal oxide semiconductor structures for p-type nonvolatile memory applications" Appl. Phys. Lett. **84**, 5079 (2004).

[11] P. Sutter, C. Schwarz, E. Müller, V. Zelezny, S. Goncalves- Conto, H. van Kanel. "Magneton sputter epitaxy of Si_mGe_n/Si(001) strained layer superlattices". Appl. Phys. Lett. **65(17),**2220, (1994).

[12] F. Ay, "Silicon based dielectric: Growth characterization and applications" Ankara, 2005, PhD Thesis

[13] T. Maruyama, M. Ichida, "Thin films of Amorphous Germanium- Nitrogen Alloys Prepared by Radio Frequency Reactive Sputtering", J. Electrochem. Soc., **146(3),** 1186, (1999).

[14] http://www.jawoollam.com

[15] A. B. Young, J. J Rosenberg and Szendro I," Preperation of Germanium Nitride Films by Low Pressure Chemical Vapor Deposition", J. Electrochem. Soc., **134 (11),** 2867, (1987).

[16] http://www2.fc.up.pt/pessoas/peter.eaton

[17] T.S. Shi,S.N. Sahu, G.S. Oehrlein, A. Hiraki and J. W. Corbett, "Models for the Hydrogen-Related Defect - Impurity Complexes and Si-H Infrared Bands in Crystalline Silicon", Phys. Status Solidi A, 74, 329 (1982).

[18] G. Bauer, W. Richter, *Optical Characterization of Epitaxial Semiconductor Layers*, Springer-Verlag, Berlin (1996).

[19] L. Chun-rong, S. Zhao-qi, X. Jing-Zhou, X. Zheng, " Infrared Absorption Bands of a Plasma-Nitrided Film on Germanium (111)", J. Phys. D: Appl. Phys., **24**, 2215, (1991)

[20] Chen Guanghua, Zhang Fangqing, "Infrared and Raman spectra of reactively sputtered amorphous GeN_x---H film",**185 (2),** 231, (1990)

[21] S. Sayan, E. Garfunkel, S. Suzer, "Soft X-Ray Photoemission Studies of The HfO2/SiO2/Si Systems", Appl. Phys. Lett., **80**, 2135, (2002).

[22] P.Y. Yu, M. Cardona, *Fundamentals of Semiconductors: Physics and Materials Properties*, Springer-Verlag, Berlin, (1996).

[23] V. A. Gritsenko, A. S. Shaposhnikov, W. M. Kwok, H. Wong, "Valence Band Offset at Silicon/Silicon Nitride and Silicon Nitride/Silicon Oxide Interfaces", Thin Solid Films, **437**, 135, (2003).

[24] S. J. Wang, J. W. Chai, J. S. Pan, A. C. H. Huan,"Thermal Stability and Band Alignments for Ge_3N_4 Dielectrics on Ge", Appl. Phys. Lett., **89(022105)**, 1, (2006).

[25] I. Chambouleyron, A.R. Zanatta, "Nitrogen in Germanium", J. Appl. Phys., **84 (1)**, 1, (1998).

[26] S. Makler, G. M. Rocha, E. V. Anda, "Electronic Structure of a-$Si_{1-x}N_x$:H and a-$Ge_{1-x}N_x$:H", Phys. Rev. B, **41**, 5857, (1990).,

[27] S. Miyazaki, "Photoemission Study of Energy-Band Alignments and Gap-State Density Distributions for High-k Gate Dielectrics", J. Vac. Sci. Technol. B, **19**, 2212, (2001)

[28] S. Süzer, S. Sayan, B. M. M. Holl, E. Garfunkel, N. M. Hamdan, Z. Hussain, "Soft X-Ray Photoemission Studies of Hf Oxidation", J. Vac. Sci. Technol. A, **21(1),** 106, (2003).

[29] E. A. Kraut, R. W. Grant, J. R. Waldrop, S. P. Kowalczyk, "Precise Determination of The Valence-Band Edge in X-Ray Photoemission Spectra: Application to Measurement of Semiconductor Interface Potentials", Phys. Rev. Lett., **44(24),** 1620, (1980).

[30] P. F. Zhang, X. L. Liu, R. Q. Zhang, H. B. Fan, A. L. Yang, H. Y. Wei, P. Jin, S. Y. Yang, Q. S. Zhu, Z. G. Wang, "Valence Band Offset of ZnO/GaAs Heterojunction Measured by X-Ray Photoelectron Spectroscopy", Appl. Phys. Lett., **92(012104),** 1, (2008)

[31] F. A. Jenkins, H.E. White, Fundamentals of optics, 4th ed. McGraw-Hill, Inc., (1981)

[32] P. Basa, P. Petrik, M. Fried, A. Dâna, A. Aydinli, S. Foss, T. G. Finstad, "Spectroscopic ellipsometric study of Ge nanocrystals embedded in SiO_2 using parametric models", Physica Status Solidi A (2007)

[33] Akhilesh K. Arora, M. Rajalakshmi, T.R. Ravindran and V. Sivasubramanian. "Raman Spectroscopy of optical phonon confinement in nanostructured materials". J. Raman Spectrosc**. 38**., 604-617, (2007).

[34] Y. M. Yang, X. L. Wu, G. S. Huang, D. S. Hu, G. G. Siu, "Confinement effect of optical phonons in Si-Ge alloy nanocrystals". Physics Letter A **(338),** 379-384, (2005).

[35] Richter H., Wang ZP., Ley L. , Solid State Commun. ,**39**, 625, (1981)

[36] Campbell H., Fauchet PM., Solid State Commun. **58**, 739, (1986)

[37] G. kartopu, S.C. Bayliss, Y. Ekinci, E.H. C. Parker, T. Naylor. "Observation of phonon confinement in SiGe nanocrystals and preferential etching of Si in porous $Si_{1-x}Ge_x$ films". Phys. Stat. Sol. (a). **197 (1),** 263, (2003).

[38] J. C. Tsang, P. M. Mooney, F. Dacol, J. O. Chu, "Measurements of alloy compositions and strain in the Ge_xSi_{1-x} layers", J. Appl. Phys. **75 (12)**, 8098, (1994)

[39] M. Holtz, W. M. Duncan, S. Zollner, R. Liu. Visible and ultraviolet Raman scattering studies of $Si_{1-x}Ge_x$ alloys. J. Appl. Phys. **88(5),** 2523, (2000)

[40] S. Rath, M. L. Hsieh, P. Etchegoin, R.A. Stradling, "Alloy effects on the Raman Spectroscopy of $Si_{1-x}Ge_x$ and calibration protocols for alloy compositions based on polarization measurements", Semicond. Sci. Technol. **18**, 566-575, (2003)

[41] Haizhou Yin, K. D. Habort, F. J. Kub, S.R. Shieh, T.S. Duffy, J. C. Sturm. " High Germanium-content SiGe islands formed on compliant oxide by SiGe oxidation". Appl. Phys. Lett. **84(18)**, 3624, (2004)

[42] S. J. Koester, K. Rim, J. O. Chu, P. M. Mooney, J. A. Ott, M.A. Hargrove. "Effect of thermal processing on strain relaxation and interdiffusion in Si/SiGe

heterostructures studied using Raman Spectroscopy". Appl. Phys. Lett. Vol **79 (14)**, 2148, (2001).

[43] Y. H. Luo, J. L. Liu, G. Jin, J. Wan, K. L. Wang. "An effective compliant substrate for low-dislocation relaxed $Si_{1-x}Ge_x$ growth". Appl. Phys.A **74,** 699-702, (2002).

[44] F. Lu, C.H.Perry, F. Namavar, N.L. Rowell, R. A. Soref. Appl. Phys. Lett. **63**,1243 (1993)

[45] E.V. Jelenkovic, K.Y. Tong, Z. Sun, C.L. Mak, W. Y. Cheung. J. Vac. Sci. Technol. A **15** ,2836 (1997)

[46] J. Olivares, P.Martin, A. Rodriguez, J. Sangrador, J. Jimenez, T. Rodriguez. "Raman spectroscopy study of amorphous SiGe films deposited by low pressure chemical vapor deposition and polycrystalline SiGe films obtained by soli-phase crystallization", Thin Solid Films, **358**, 56-61, (2000).